

Analysis of Mesoscale Airflow Patterns in the South-Central Coast Air Basin during the SCCAMP 1985 Intensive Measurement Periods

SHARON G. DOUGLAS AND ROBERT C. KESSLER

Systems Applications, Inc., San Rafael, California

(Manuscript received 25 January 1990, in final form 22 August 1990)

ABSTRACT

An analysis of the mesoscale airflow patterns in the south-central coast air basin (SCCAB) was performed using data collected during the 1985 South-Central Coast Cooperative Aerometric Monitoring Program (SCCCAMP). Airflow within the SCCAB is strongly influenced by the diurnal sea-breeze/land-breeze cycle and by slope flows that develop along the steep terrain. Mesoscale airflow features observed during the four intensive monitoring periods include eddies along the coast and over the Santa Barbara Channel. An analysis of the transport patterns indicated that both recirculation of pollutants within the SCCAB and transport of pollutants from the south coast air basin (SOCAB) contributed to the observed high ozone concentrations on the intensive monitoring days.

1. Introduction

Wind data collected during the 1985 South-Central Coast Cooperative Aerometric Monitoring Program (SCCCAMP) were used to analyze the mesoscale airflow patterns in the south-central coast air basin (SCCAB) during four intensive monitoring periods: 12–14 September, 20–21 September, 23–25 September, and 2–4 October. A large number of surface and upper-air monitoring sites were operated during the SCCCAMP and were primarily located within the coastal and offshore areas.

An understanding of the mesoscale airflow patterns is critical to understand ozone episodes in the SCCAB. Since high ozone concentrations were observed in the SCCAB during three of the four intensive monitoring periods, the SCCCAMP data provided the opportunity to improve our understanding of the mesoscale airflow associated with ozone episodes. The large number of monitoring sites provided good spatial and temporal resolution of some mesoscale airflow features. The SCCCAMP wind data are summarized in section 2.

The wind data were analyzed using a diagnostic wind model. Using this model observational wind data are incorporated via weighted interpolation into a first-guess field that consists of a domain-mean wind that has been adjusted for terrain effects. Figure 1 illustrates the complex topography of the SCCCAMP wind analysis domain. The diagnostic wind model is described in section 3.

A number of interesting airflow patterns was observed during the intensive monitoring periods, including the development of mesoscale eddies along the coast and over the Santa Barbara Channel. The complex mesoscale airflow patterns in the SCCAB govern the transport of ozone and ozone precursors within the region and through its boundaries. Ozone precursor emissions within the SCCAB are concentrated in the Ventura-Oxnard, Santa Barbara, and offshore areas. The south coast air basin (SOCAB), located to the southeast of the SCCAB, is also a potential source of ozone and ozone precursors. Los Angeles is situated within the SOCAB.

Backward particle paths were generated using the analyzed wind fields to assess possible transport of ozone and ozone precursors during the four intensive monitoring periods. The mesoscale airflow patterns and particle path analyses are presented in section 4. The analysis results are summarized in section 5.

2. Wind data

The SCCCAMP wind analysis domain and the locations of the surface and upper-air wind monitoring sites are shown in Fig. 2. Note that the observation density at the surface (especially along the coastline) is much greater than that aloft. The existing meteorological monitoring network in the SCCAB was supplemented to enable the characterization of pollutant transport in the Santa Barbara Channel, coastal areas of Santa Barbara County, and the southern portion of Ventura County (Dabberdt and Vezee 1987). In general, hourly averaged wind data were reported at the surface monitoring sites. The upper-air monitoring network consisted of radiosondes (with measurements

Corresponding author address: Ms. Sharon Douglas, Systems Applications, Inc., 101 Lucas Valley Road, San Rafael, CA 94903.

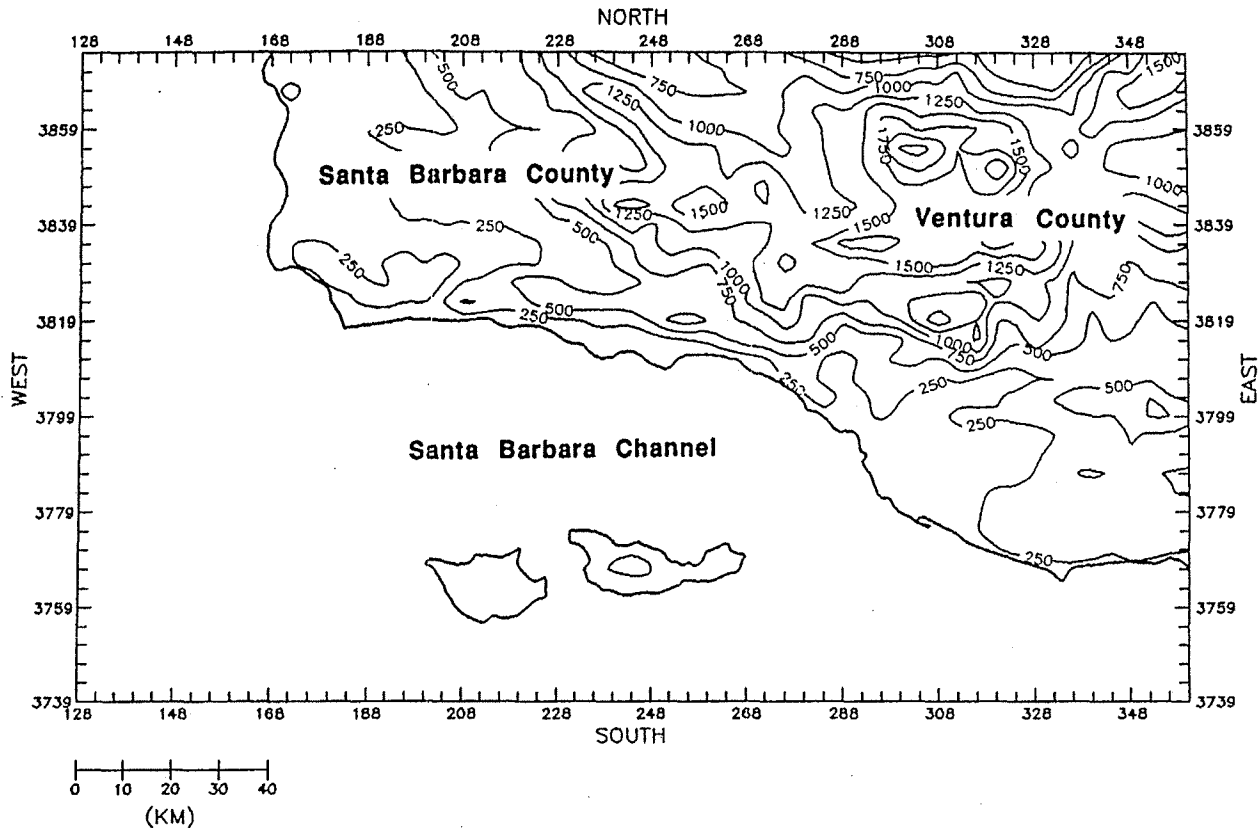


FIG. 1. The SCCAMP wind analysis domain. The axes are labeled in zone 11 Universal Transverse Mercator (UTM) coordinates. Topography is contoured in meters.

2–4 times daily) and Doppler acoustic sounders (with continuous measurements).

3. Diagnostic wind model

Hourly gridded wind fields were generated for each of the intensive monitoring days using a diagnostic wind model (Kessler et al. 1988). This model incorporates observations where they are available and provides some information on terrain-induced airflows in regions where local observations are absent. The model is formulated in terrain-parallel coordinates. Wind fields are generated using a two-step procedure.

In step 1, a domain-scale mean wind is adjusted for terrain effects. These include the kinematic effects of terrain (the lifting and acceleration of the airflow over terrain obstacles), thermodynamically generated slope flows, and blocking effects. Step 1 produces a spatially varying gridded field of u and v for each vertical layer within the model domain.

Step 2 adds observational information to the (u, v) field calculated in step 1 by using an objective analysis procedure: observations are used within a user-specified radius of influence, while the step 1 (u, v) field is used in subregions where observations are unavailable. The following modified inverse-distance-squared weighting

scheme (Ross and Smith 1986) is used for the interpolation of data:

$$(u, v)_2 = \left\{ \sum_k [r_k^{-2}(u_0, v_0)_k] + R^{-2}(u, v)_1 \right\} / \left(\sum_k r_k^{-2} + R^{-2} \right) \quad (1)$$

where (u_0, v_0) denotes an observed wind at station k , r_k is the distance from station k to a given grid point, $(u, v)_1$ is the step 1 wind field at the grid point, and $(u, v)_2$ is the updated wind vector. The parameter R controls the relative influence of the observations and the step 1 wind field. The weighting scheme is illustrated graphically in Fig. 3.

Following the interpolation, a 5-point smoother in the form:

$$A'_{i,j} = 0.5A_{i,j} + 0.125(A_{i-1,j} + A_{i+1,j} + A_{i,j-1} + A_{i,j+1}) \quad (2)$$

is applied to the horizontal wind field to reduce the discontinuities that may result from the interpolation. The vertical velocity is calculated by integrating the incompressible conservation of mass equation. Zero-gradient lateral boundary conditions are used.

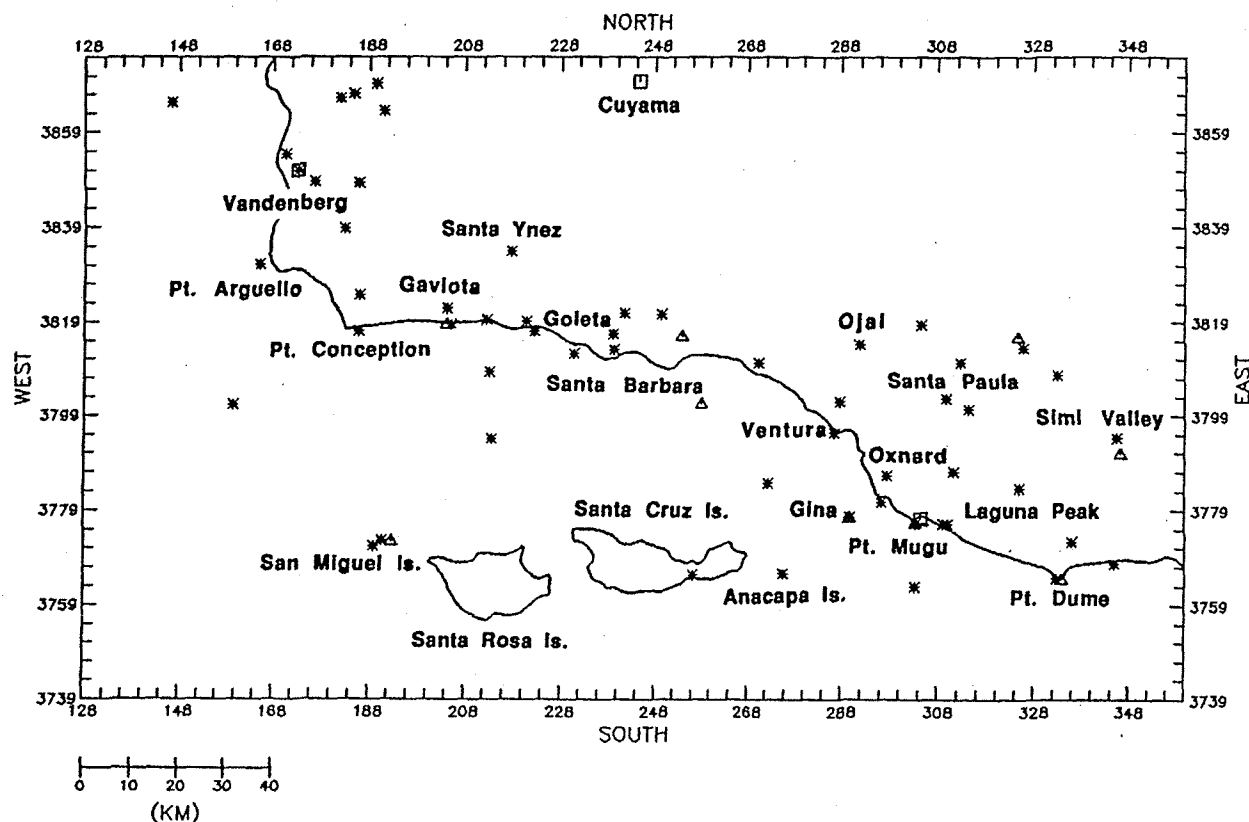


FIG. 2. The SCCAMP monitoring network. The locations of the surface wind monitoring sites are denoted by asterisks. Upper-air radiosonde site locations are denoted by squares and Doppler acoustic sounder site locations are denoted by triangles.

Generation of the SCCAMP wind fields involved 1) preprocessing of the wind data for input into the model, 2) specification of model input parameters, and 3) exercise of the diagnostic wind model. Winds were analyzed within each of five vertical layers: 0–20, 20–180, 180–420, 420–780, and 780–1220 m AGL. The nominal analysis levels of 10, 100, 300, 600, and 1000 m AGL referenced in the discussion represent the midpoints of these layers.

In the preprocessing step, the upper-air data were vertically averaged within the model layers and the less-frequent upper-air data were linearly interpolated in time to enhance the temporal consistency of the wind fields and to provide hourly input for the diagnostic wind model.

Maximum radii of influence for the interpolation of data were based on the spatial distribution of observations and were assigned values of 20 km for the surface layer, 50 km aloft, and 200 km over water. The weighting parameter for the terrain effects (R) was set equal to 10 km in the analysis of the surface winds and 25 km in the analysis of the winds aloft. Kessler et al. (1988) discuss the tests that were performed to examine the sensitivity of the diagnostic wind model to the various controlling parameters and to determine the op-

timum values of these parameters for the SCCAMP wind analysis.

The diagnostic wind model also requires, as input, domain-mean wind and domain-scale stability information. For this analysis, specification of the hourly domain-mean wind was based upon the Cuyama ra-

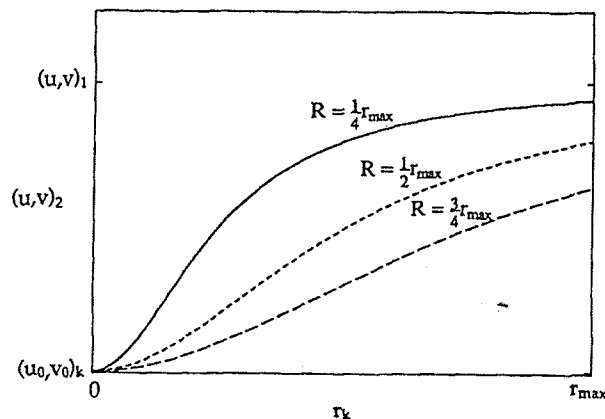


FIG. 3. Graphical illustration of the interpolation scheme for a single observation.

diosounding, which was located at 244.5 easting and 3870.0 northing in Universal Transverse Mercator (UTM) zone 11. Data from this site were selected to represent the wind in the portion of the domain where the first-guess field of the diagnostic wind model was weighted most heavily (the data-sparse interior). Similarly, the specification of the domain-mean lapse rate was based on the Cuyama sounding. Since this station is located well inland, it is unlikely that it is influenced by the advection of maritime lapse rates.

The accuracy that the diagnostic wind model represents the wind field at a given grid point depends upon nearby wind observations, the terrain-adjusted wind field at that grid point, and the radius of influence and other controlling parameters. Experiments demonstrating the accuracy of the diagnostic wind model are described by Kessler et al. (1988).

4. Intensive monitoring periods

This section contains an overview of the synoptic-scale meteorology, an analysis of the mesoscale airflow patterns, a summary of the ozone air quality, and an examination of possible transport patterns for each of the intensive monitoring periods. A comprehensive summary of the synoptic-scale meteorology during SCCAMP 1985 is given by Viezee et al. (1987). Detailed descriptions of the mesoscale airflow patterns are provided by Kessler et al. (1988). An overview of the ozone air quality during the intensive monitoring periods is given in Table 1.

In this section the airflow patterns are illustrated by plots of the analyzed wind fields at 1500 PDT for the surface layer (10 m AGL) and layer 3 (300 m AGL).

a. 12–14 September

1) SYNOPTIC OVERVIEW

Eastward movement of the Pacific high and advection of warm air into southern California by a hurricane located southeast of Baja California resulted in significant warming of the troposphere on 12 September. Building high pressure at the surface produced subsidence and inversion conditions within the SCCAB. This warming did not continue into 13 September because of the development of a low pressure trough along the West Coast and a retreat westward of the Pacific

high. Weak pressure gradients and light winds characterized the SCCAMP study area. A cold front associated with the low pressure system off the coast of Washington was approaching from the north. On 14 September the low pressure system weakened and moved inland while northwesterly winds began developing along the California coast.

2) MESOSCALE AIRFLOW PATTERNS

Diagnostic analyses of the airflow patterns for 12–14 September at the surface and 300 m AGL are presented in Figs. 4–6.

The airflow within the SCCAB during the morning of 12 September was characterized both at the surface and aloft by offshore-directed drainage and downslope flow along the coast, northeasterly flow over the inland portion of the domain, and northwesterly flow in the southwestern part of the domain. During the early morning hours, winds over the central Santa Barbara Channel were calm.

A sea breeze developed along most of the coastline by 1200 PDT, persisted through 1800 PDT, and penetrated inland as far as 50 km. The analysis of sea-breeze penetration may be limited by lack of available data in areas far removed from the coastline. The 1500 PDT surface analysis (Fig. 4a) illustrates the extent of sea-breeze penetration. Western Santa Barbara County, Ojai, and the Oxnard plain are under the influence of the sea breeze.

A common feature of the airflow in the SCCAB is the persistent northwesterly flow along the western edge of Santa Barbara County. Curvature effects introduced by the coastal curvature in the vicinity of Point Arguello/Point Conception often combine with onshore/upslope flow along the Santa Barbara coast to form an eddy in the Gaviota area. This eddy, frequently referred to as the Gaviota eddy (Smith et al. 1983), is indicated in the 1500 PDT surface analysis. A weaker sea breeze with less inland penetration than at the surface is indicated at 300 m AGL (Fig. 4b). Winds at this level were weaker in many areas.

During the evening of 12 September, onshore flow at the surface was gradually replaced by nocturnal drainage flow. This offshore-directed flow was somewhat weaker than on the previous day. North-northwest winds persisted in the western portion of the anal-

TABLE 1. Overview of ozone air quality during the SCCAMP intensive monitoring periods.

Period	Peak ozone concentration (pphm)	Peak concentration time (end hour)	Peak concentration location
12–14 September	19.2	1500 PDT 13 September	Laguna Peak
20–21 September	9.5	1400 PDT 21 September	Castro Peak
23–25 September	23.0	1600 PDT 24 September	Goleta
2–4 October	20.5	1600 PDT 3 October	Platform Gina

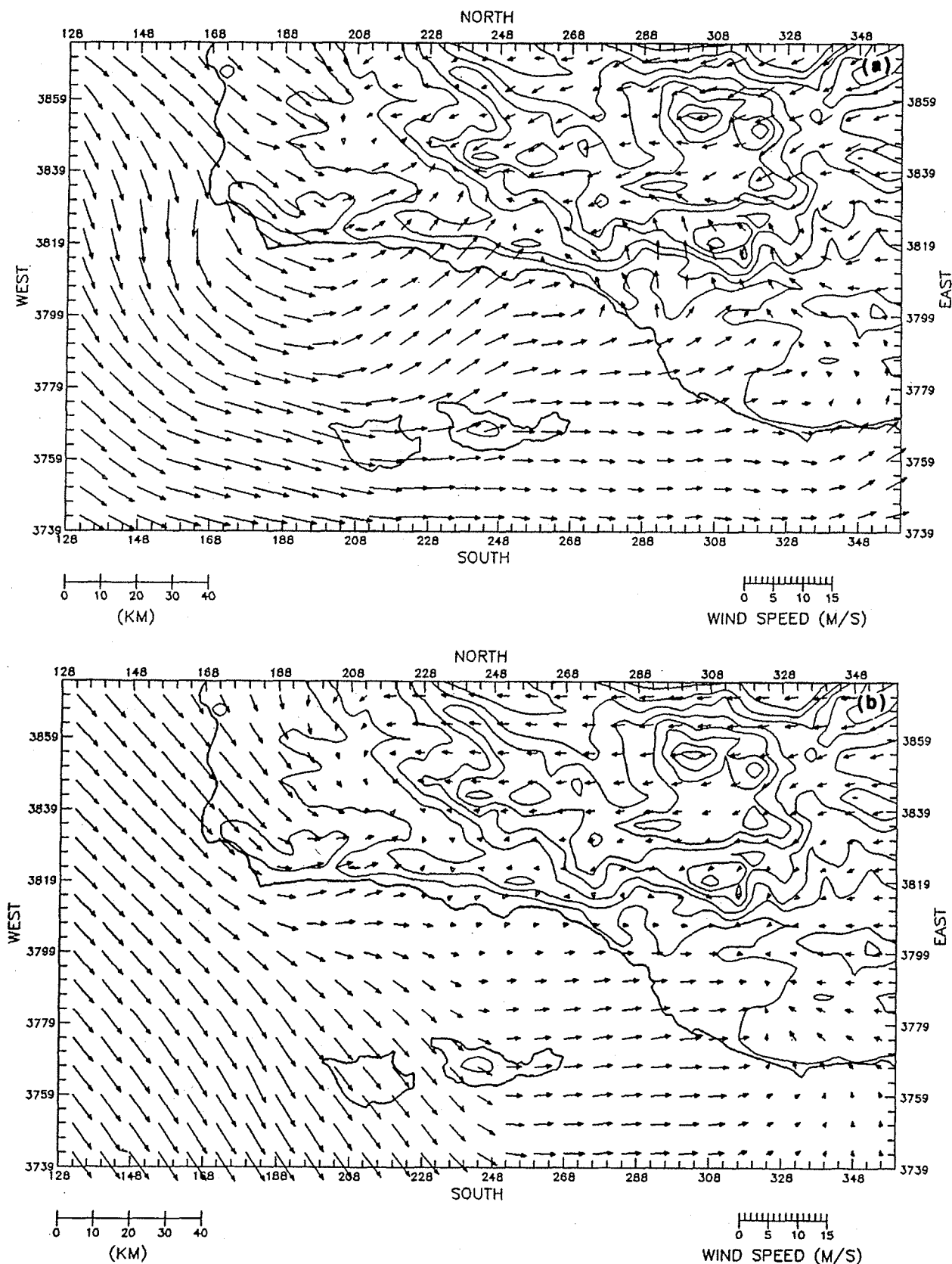


FIG. 4. Diagnostic wind fields for 1500 PDT 12 September 1985 at (a) 10 m AGL, and (b) 300 m AGL.

ysis domain throughout the night. At 300 m AGL, the morning airflow was characterized by easterly flow throughout much of the domain, with southeasterly flow over midchannel, and northerly flow in the western part of the domain.

Sea-breeze development on 13 September was similar to that on 12 September, but with greater inland penetration. The 1500 PDT surface analysis (Fig. 5a) shows that the influence of the sea breeze extended to Simi Valley in Ventura County. A partial Gaviota eddy is indicated on this day. The extent of the onshore flow at 300 m AGL was also greater on 13 September especially in Ventura County (Fig. 5b). The depth of the sea breeze appears to have exceeded 600 m (Kessler et al. 1988). The alongshore component of the flow intensified throughout the remainder of the afternoon both at the surface and aloft.

The retreat of the sea breeze and the development of nocturnal drainage flow on the evening of 13 September resulted in offshore-directed flow and a convergence zone in midchannel during the morning of 14 September. The 300-m AGL wind field was characterized by southeasterly flow over the channel and northwesterly flow in the western portion of the domain.

Strong sea-breeze development occurred in Ventura County and along the western end of Santa Barbara County on the afternoon of 14 September. In the Santa Barbara area, the 1500 PDT surface analysis (Fig. 6a) indicates a sharp offshore convergence zone that was formed by strong northwesterly flow in the Gaviota area (apparently an extension of the sea breeze from the western end of Santa Barbara County), southwesterly flow to the north of Santa Rosa Island, and southeasterly flow just southwest of Santa Barbara. In Ventura County the inland penetration of the sea-breeze front appears to be more rapid than on the previous two days affecting both Simi Valley and Ojai by 1000 PDT. The effects of the synoptic forcing are clearly seen at 300 m AGL (Fig. 6b), which was characterized by strong northwesterly flow in the western half of the domain and primarily westerly flow in the eastern half of the domain.

3) OZONE AIR-QUALITY SUMMARY

No exceedances of the National Ambient Air Quality Standard (NAAQS) for ozone, 12 parts per hundred million (pphm), were recorded on 12 September. The warming of the troposphere on this day was associated with increasing ozone and a maximum concentration of 10 pphm at South Mountain. Ozone levels rose sharply on 13 September in both counties but especially in Ventura County. The maximum concentration recorded on this day was 19 pphm at Laguna Peak. A decrease in ozone concentrations was observed on 14 September, but ozone levels remained high at some high-elevation sites.

4) TRANSPORT PATTERNS

Backward particle paths were calculated to examine the possible transport of ozone and ozone precursors within the SCCAB. The particle paths were calculated by first interpolating the analyzed wind fields to the particle position, advecting the particle backward in time for a given time interval, and then integrating the distance traveled by the particle during each time interval. A time interval equal to 15 min was used. To illustrate possible transport patterns during the intensive monitoring periods, backward particle paths were calculated for selected monitoring sites for a 12-h period ending with the hour that the peak ozone concentration was recorded at the site. The backward particle paths were calculated for the surface layer (10 m AGL) and layer 3 (300 m AGL). The two-dimensional particle paths do not incorporate vertical motion, which may be a source of error considering the mesoscale regimes present in the study area.

Backward particle paths for the 12–14 September intensive study period are presented in Fig. 7. The highest ozone concentrations for this intensive monitoring period occurred on 13 September in Ventura County. Five sites within Ventura County were selected for the calculation: Castro Peak, Simi Valley, Laguna Peak, South Mountain, and Santa Paula. Maximum ozone concentrations and peak concentration times (hour end) for each of the monitoring sites are given in Fig. 7a.

The surface-layer particle paths (Fig. 7a) indicate that particles arriving at Santa Paula, South Mountain, and Laguna Peak at 1500 PDT on 13 September were positioned over the Santa Barbara Channel 12 h earlier. Particles arriving at Castro Peak at 1400 PDT and Simi Valley at 1500 PDT appear to have been recirculated by the diurnal land-breeze/sea-breeze cycle. The particles were carried offshore during the early morning hours and returned to shore with the sea breeze, which developed between 900 and 1000 PDT along the Ventura coast. The surface-layer particle paths suggest that intrabasin transport from sources both onshore and offshore may have contributed to the high ozone concentrations observed in Ventura County on 13 September.

At 300 m AGL (Fig. 7b), the backward particle paths indicate possible interbasin transport from the SOCAB via an overwater route. Observed high ozone concentrations at elevated monitoring sites support upper-level ozone transport. Pollutants transported aloft may be mixed down to the surface through convective mixing.

b. 20–21 September

1) SYNOPTIC OVERVIEW

Synoptic-scale conditions on 20 September were characterized by building high pressure over the eastern Pacific, subsidence and warming of the lower tropo-

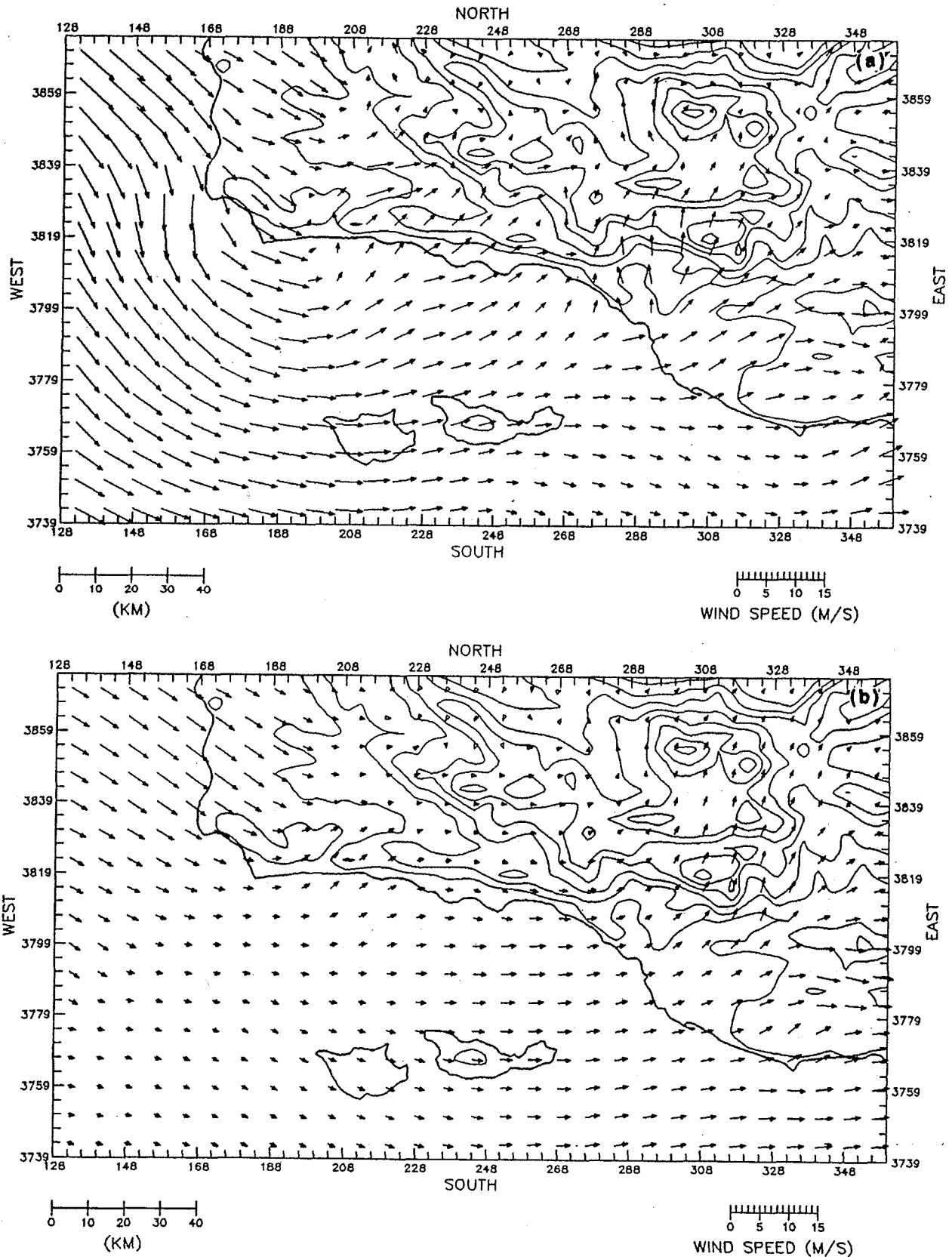


FIG. 5. As in Fig. 4, but for 13 September 1985.

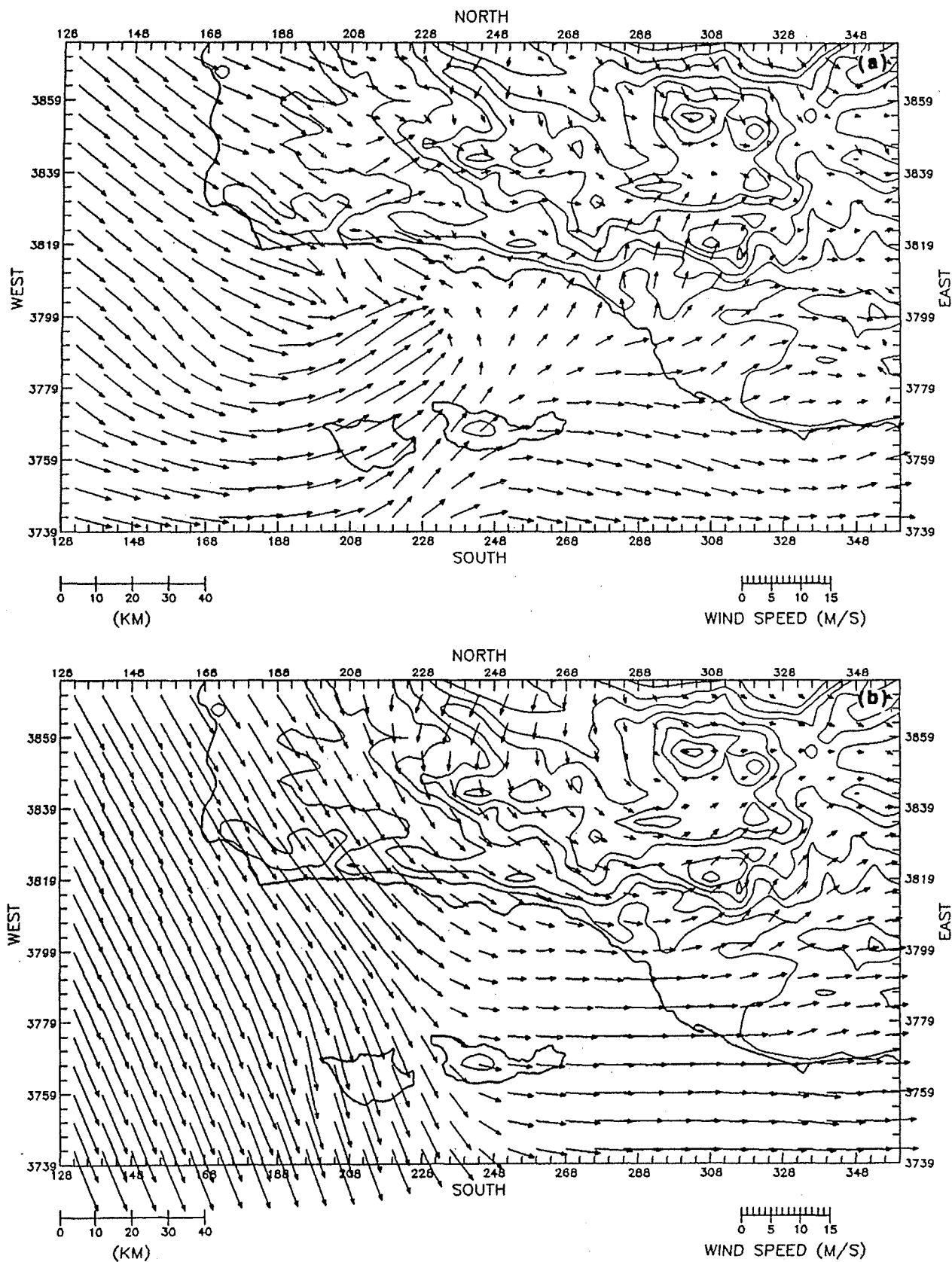


FIG. 6. As in Fig. 4, but for 14 September 1985.

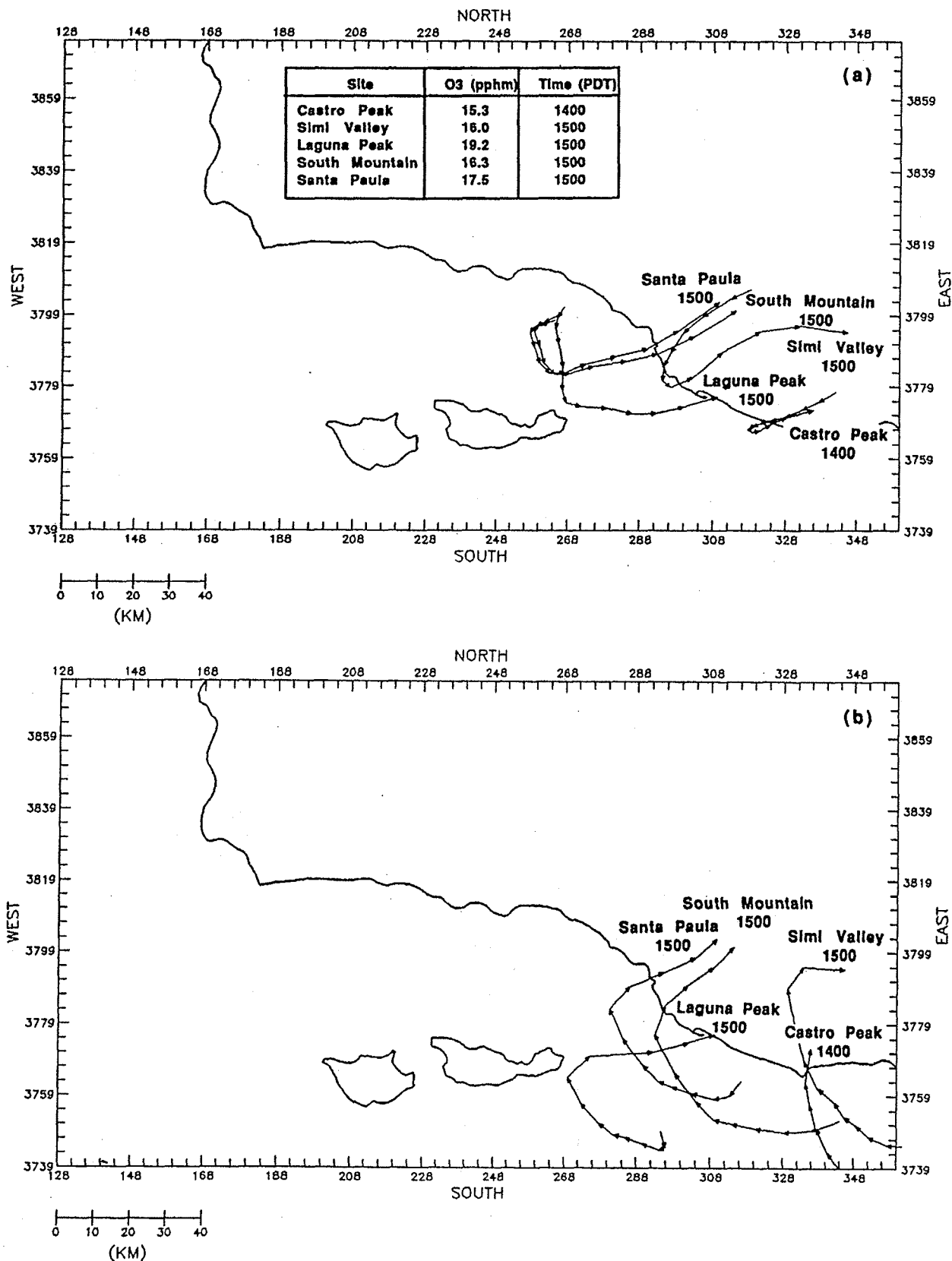


FIG. 7. Backward particle paths for 13 September 1985 at (a) 10 m AGL and (b) 300 m AGL. The particle paths were calculated using the diagnostic wind fields. Maximum ozone concentrations and peak concentration times are given for each of the receptor sites.

sphere, and strong inversion conditions. Conditions were favorable for the development of an ozone episode, but a cold-air outbreak from Canada on 21 September, combined with persistent low pressure over southern California at 500 mb, halted the development of conditions favorable for high oxidant concentrations in the SCCAB (Viezee et al. 1987).

2) MESOSCALE AIRFLOW PATTERNS

Diagnostic analyses of the airflow patterns for 20–21 September at the surface and 300 m AGL are presented in Figs. 8 and 9.

Surface analyses for the morning of 20 September indicate northeasterly flow inland, weak drainage winds along the coast, and numerous zones of convergence and divergence over the channel. At 0300 PDT convergence is indicated off the coast near Ventura and to the southwest of Point Dume. Eddy development is indicated over the western channel between 0500 and 0900 PDT until the onset of the sea breeze at approximately 0900 PDT. Winds aloft were primarily northerly, with easterly flow emerging in the southeastern corner of the domain. This easterly flow intensified, propagated westward, and veered south throughout the morning. Superposition of northwesterly flow in the western half of the domain and southeasterly–southerly flow in the eastern half of the domain produced an eddy that was positioned over the Santa Barbara Channel between 0900 and 1200 PDT.

The 1500 PDT surface analysis (Fig. 8a) shows a well-developed sea-breeze regime. Sea-breeze penetration of up to 50 km inland is indicated in both Ventura and western Santa Barbara counties. The presence of the Gaviota eddy is indicated. The depth of the sea breeze exceeded 300 m over Ventura County during the afternoon of 20 September (Fig. 8b) and contributes to the formation of an eddy over western Ventura County.

The retreat of the sea breeze and the subsequent development of drainage/downslope flow along the coast of Santa Barbara County lead to reformation of an eddy in the western Santa Barbara Channel by 0300 PDT 21 September. At 300 m a transition from northwesterly to northerly to easterly flow over the channel occurred overnight and may have contributed to the eddy development.

The surface-layer eddy propagated eastward and dissipated with the onset of the sea breeze, which occurred at approximately 0900 PDT. On the afternoon of 21 September, the marine air penetrated inland to Santa Ynez and Ojai by 1200 PDT and to Simi Valley by 1400 PDT (Fig. 9a). Alongshore (westerly) flow developed at 300 m AGL by 1200 PDT and intensified throughout the afternoon (Fig. 9b).

3) OZONE AIR-QUALITY SUMMARY

No exceedances of the NAAQS for ozone were recorded in the SCCAB on 20 or 21 September.

4) TRANSPORT PATTERNS

Analysis of this intensive monitoring period provides the opportunity to examine meteorological conditions that do not lead to high ozone concentrations in the SCCAB. On 21 September, ozone concentrations near 9 pphm were found throughout the region.

Backward particle paths were calculated for monitoring sites Castro Peak, Laguna Peak, West Cassitas Pass, LaCumbre Peak, and Exxon B and are presented in Fig. 10. Maximum ozone concentrations and peak concentration times (hour end) for the monitoring sites are given in Fig. 10a. Castro Peak and West Cassitas Pass experience maximum concentrations at 1400 PDT, Laguna Peak at 1500 PDT, Exxon B at 1900 PDT, and LaCumbre Peak at 2100 PDT. The lateness of the latter maxima indicates that some transport may have occurred.

Within the surface layer (Fig. 10a) particles arriving at the four coastal sites appear to have been advected alongshore and then onshore. At LaCumbre Peak, located approximately 15 km inland, advection from the northeast is indicated. The layer-3 particle paths (Fig. 10b) illustrate the effect of northerly flow inland and westerly flow over the channel. The particle paths for this intensive monitoring period indicate that the advection of clean air from the north and from over the ocean is associated with this nonexceedance day.

c. 23–25 September

1) SYNOPTIC OVERVIEW

Synoptic-scale conditions on 23 September were characterized by weak gradients and light winds both at the surface and aloft. Warming of the lower troposphere was observed on this day with the 850-mb temperature reaching 19°C. This warming trend continued into 24 September, and can be attributed to warm air advection produced by high pressure inland and a tropical depression located south of the area of interest. Both the Vandenburg and Point Mugu soundings indicate strong low-level subsidence inversions on 24 September. By 25 September the low pressure center off the coast had moved to a position southwest of the SCCAB, and the airflow shifted from the southeast to southwest. Cooling of the lower troposphere occurred.

2) MESOSCALE AIRFLOW PATTERNS

Diagnostic analyses of the airflow patterns for 23–25 September at the surface and 300 m AGL are presented in Figs. 11–13.

Weak drainage flow, light winds over the Santa Barbara Channel, and north-northwest winds in the western portion of the domain characterized the surface-layer wind fields in the SCCAB on the morning of 23 September. At 0300 PDT, a partial eddy is indicated in the western channel. The 300-m AGL analysis for this time shows easterly–northeasterly flow over the

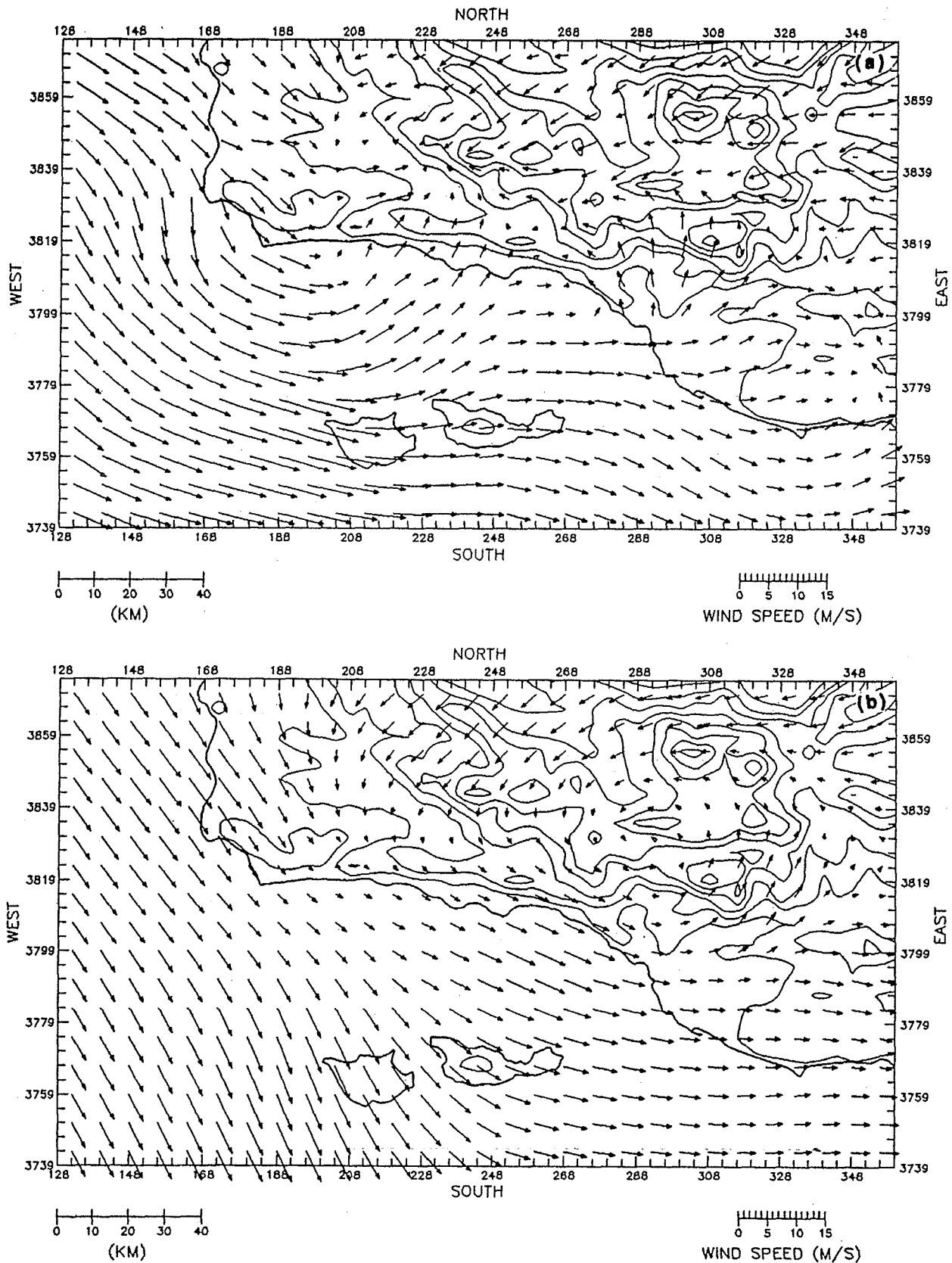


FIG. 8. As in Fig. 4, but for 20 September 1985.

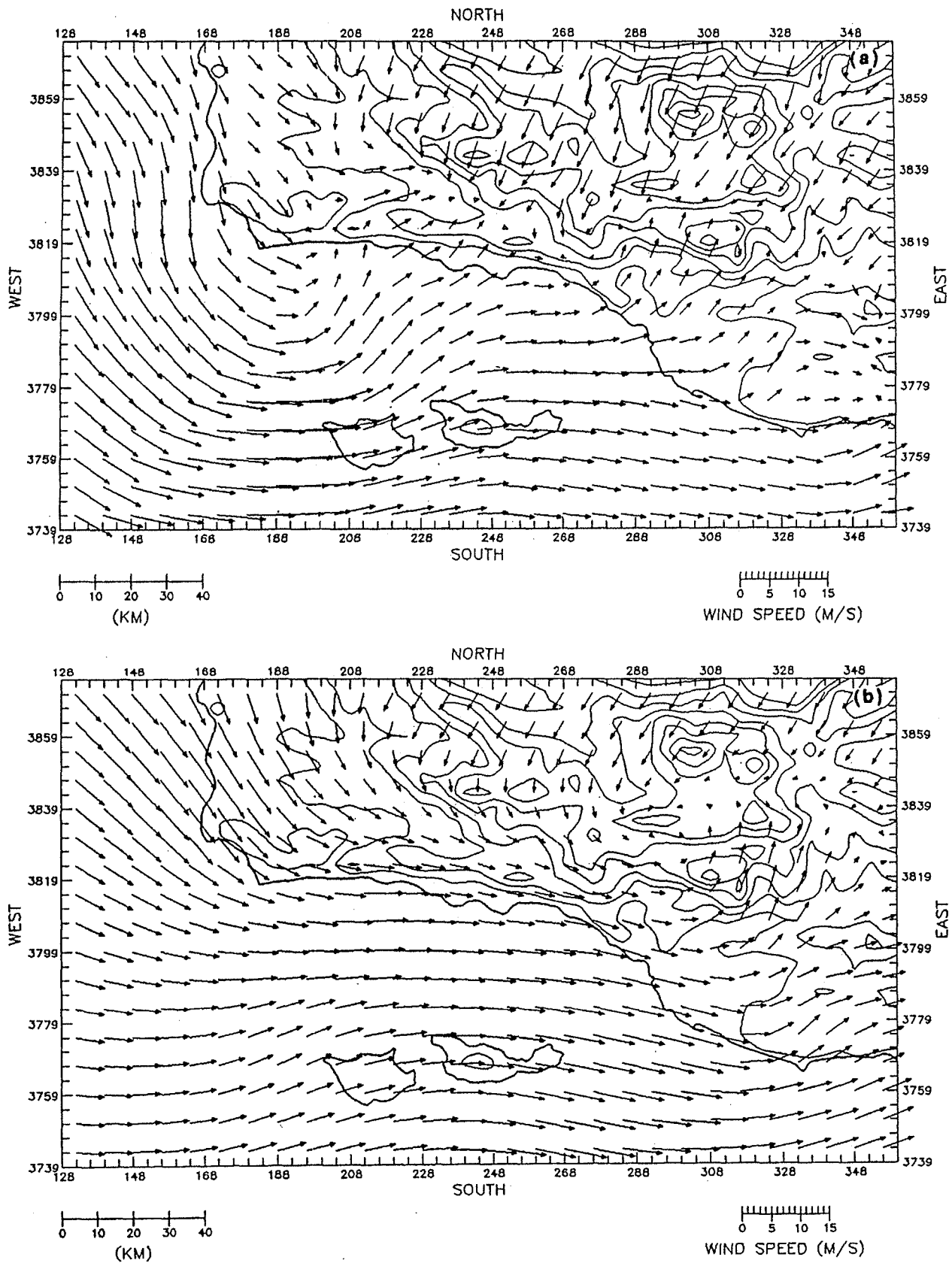


FIG. 9. As in Fig. 4, but for 21 September 1985.

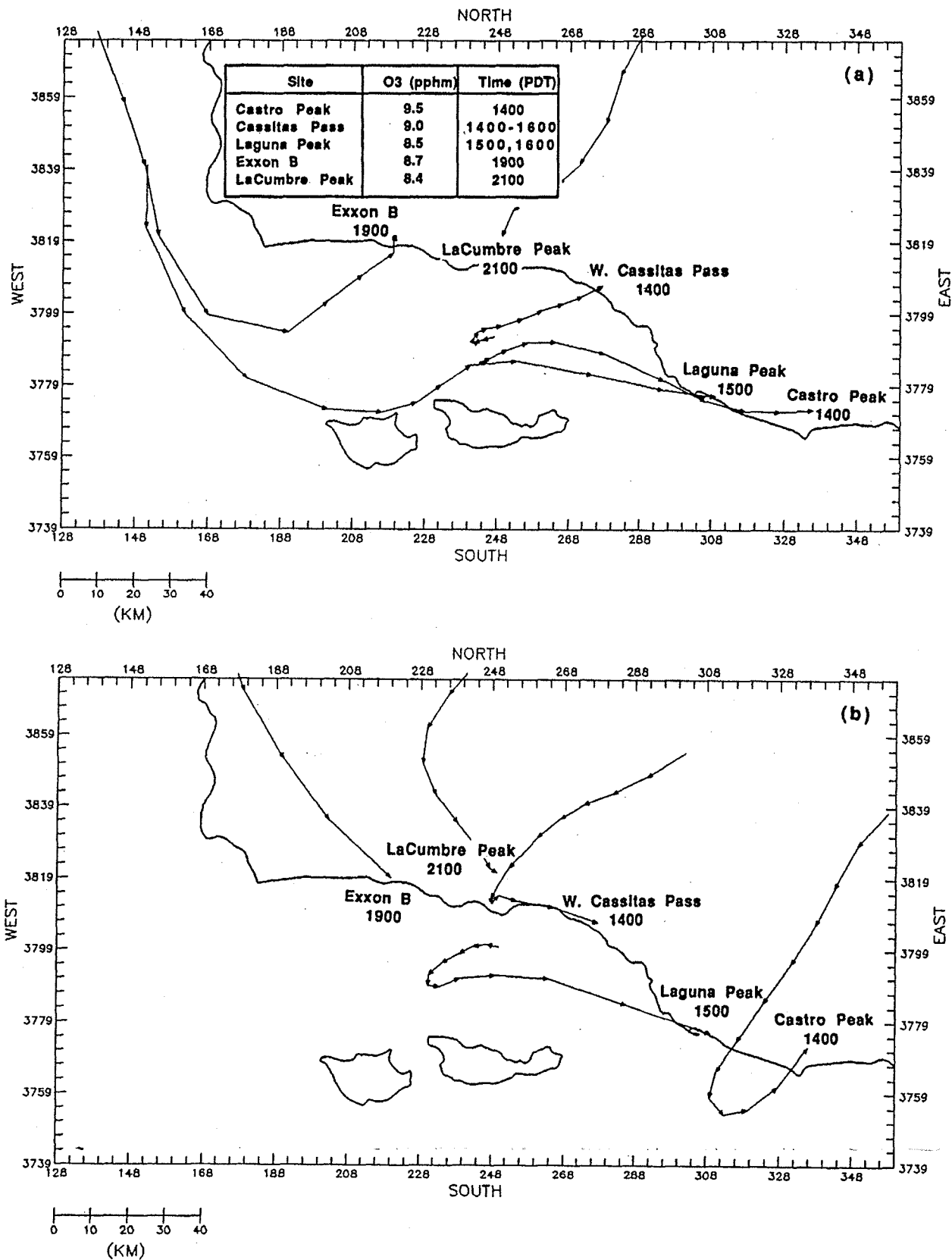


FIG. 10. As in Fig. 7, but for 21 September 1985.

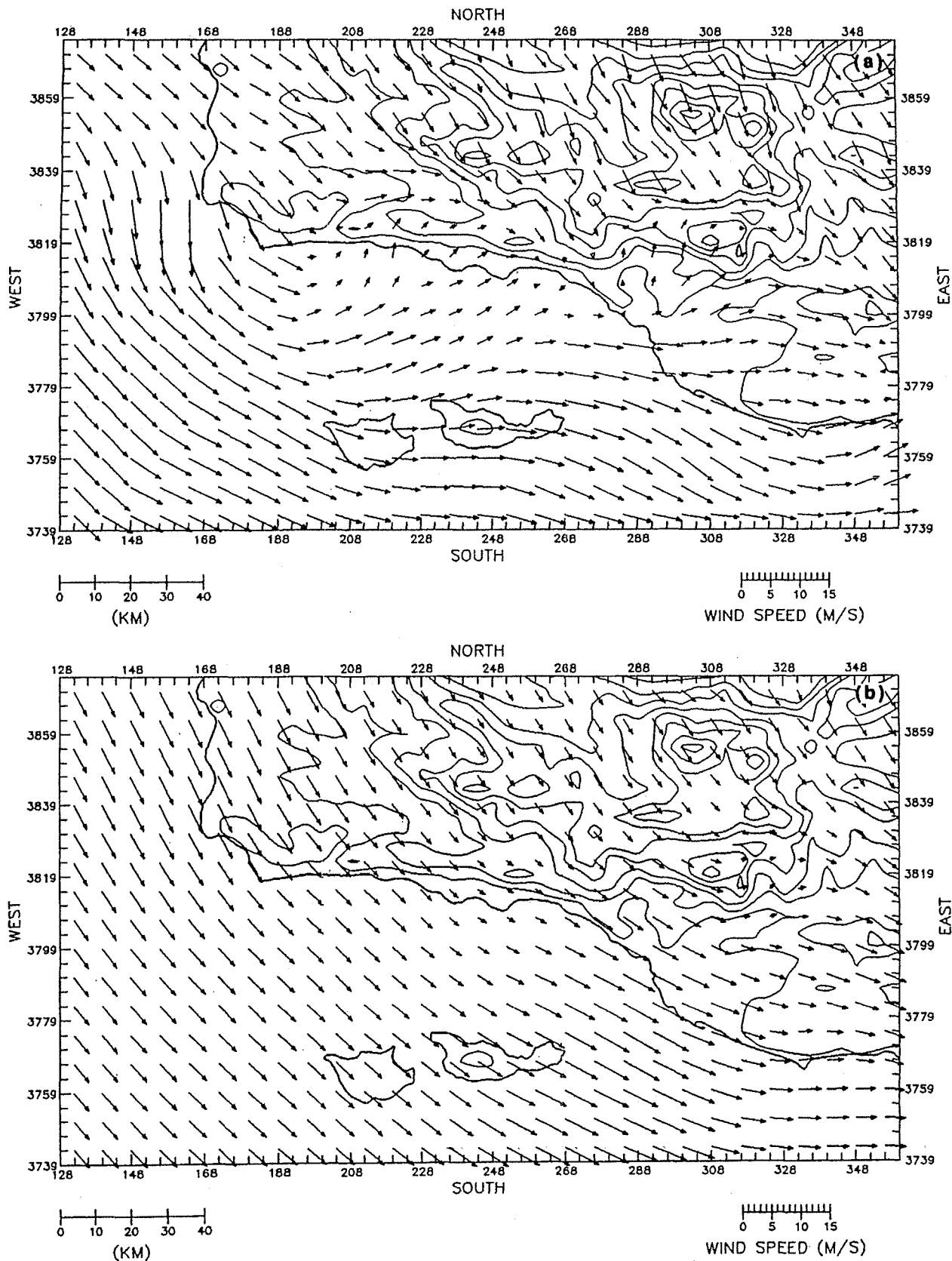


FIG. 11. As in Fig. 4, but for 23 September 1985.

eastern two-thirds of the domain and northerly-northwesterly flow over the western part of the domain.

The sea-breeze regime began to develop by 0800 PDT. This was indicated at the surface by onshore flow and a partial eddy along the coast near Gaviota. The 1500 PDT surface analysis (Fig. 11a) shows significant sea-breeze penetration that is assisted by northwesterly flow inland. Aloft the transition to westerly/alongshore flow began at approximately 1200 PDT. By 1500 PDT (Fig. 11b) northwesterly flow dominated the 300-m wind field.

The surface-layer airflow patterns for the evening of 23 September indicate northeasterly flow inland, retreat of the sea breeze and development of downslope/drainage flow along the coast, and mesoscale eddy development over the channel. During the morning of 24 September, winds over the channel were light with a northerly component. At 300 m AGL easterly flow developed in the southeastern corner of the domain before 0000 PDT and propagated northward and westward reaching the western domain boundary at 0600 PDT.

During the afternoon of 24 September the airflow within the SCCAB was influenced by a tropical depression located to the south of the study area. At the surface southerly flow began to develop over the channel before 1200 PDT and by 1500 PDT extended well inland, suggesting a modified sea breeze (Fig. 12a). Northwestery flow persisted along the west coast of Santa Barbara County forming a convergence zone between southerly and northwesterly flow in the southwestern portion of the domain. The airflow over the western channel was strongly divergent. Aloft the flow also veered toward the south during the late morning and early afternoon and by 1500 the 300-m AGL airflow over the channel was southerly (Fig. 12b). Easterly flow persisted over land and northwesterly flow (guided by the upper-air observation at Vandenberg) continued in the northwestern corner of the domain.

Subsequent analyses indicate that the development of drainage flow along the coast confined the southerly flow at the surface to the southernmost portion of the domain overnight while southeasterly flow continued at the 300-m AGL level. The convergence zone in the southwestern part of the domain persisted at the surface.

Southerly-southeasterly flow was reestablished over the channel by 1200 PDT on 25 September and by 1500 PDT (Fig. 13a) encompassed much of the domain. Southeasterly flow continued at 300 m AGL (Fig. 13b), although winds in the eastern half of the domain became southerly.

3) OZONE AIR-QUALITY SUMMARY

Ozone concentrations within the SCCAB were relatively high on 23 September, with a peak concentra-

tion of 13 pphm. On 24 September ozone levels increased sharply, and numerous exceedances of the NAAQS for ozone were recorded in both Santa Barbara and Ventura counties. On this day a peak ozone concentration of 23 pphm was recorded at Goleta.

4) TRANSPORT PATTERNS

Easterly and southerly winds along the southeastern boundary of the analysis domain and time-staggered northward-moving ozone maxima on 24 September suggest that transport from the SOCAB to the SCCAB occurred on this day. Backward particle paths were calculated for South Mountain, Ojai, Santa Barbara, Goleta, and Santa Ynez and are presented in Fig. 14. Maximum ozone concentrations and peak concentration times (hour end) are given in Fig. 14a. Peak concentrations were recorded at South Mountain, Ojai, and Santa Barbara at 1500 PDT; at Goleta at 1600 PDT; and at Santa Ynez at 1700 PDT.

Surface-layer particle paths (Fig. 14a) arriving at South Mountain and Ojai at the peak concentration times were positioned over southern Ventura County 12 h earlier. They were carried offshore and then back onshore with the southerly flow. The particle for Santa Barbara originated in western Ventura County 12 h earlier and was carried offshore and then northward along the coast. Particles arriving at Goleta and Santa Ynez at peak concentration times were advected inland from over the Santa Barbara Channel.

At 300 m AGL particle paths for 24 September (Fig. 14b) clearly indicate transport from the east and south. The orientation of the particle paths suggest that westward transport of ozone and precursor pollutants during the early morning hours may have contributed to high ozone concentrations in Santa Barbara county. As the wind shifted to the south during the afternoon, monitoring sites in Ventura County may have experienced additional transport from the SOCAB via an overwater route. Aircraft observations confirm that high ozone concentrations were found within the 200–400 m AGL layer over southeastern Ventura County and offshore during the afternoon of 24 September.

d. 2–4 October

1) SYNOPTIC OVERVIEW

Intrusion of the Pacific high into the northwestern United States and its subsequent southward movement on 2 October generated northeasterly flow aloft along the coast of California. At the surface a deep thermal trough dominated over the state. The Vandenberg sounding indicated strong low-level inversion conditions in the SCCAB. Warming of the lower troposphere continued into 3 October. A low-pressure system located to the west of Baja California may have affected the airflow in the SCCAB. On the following day this

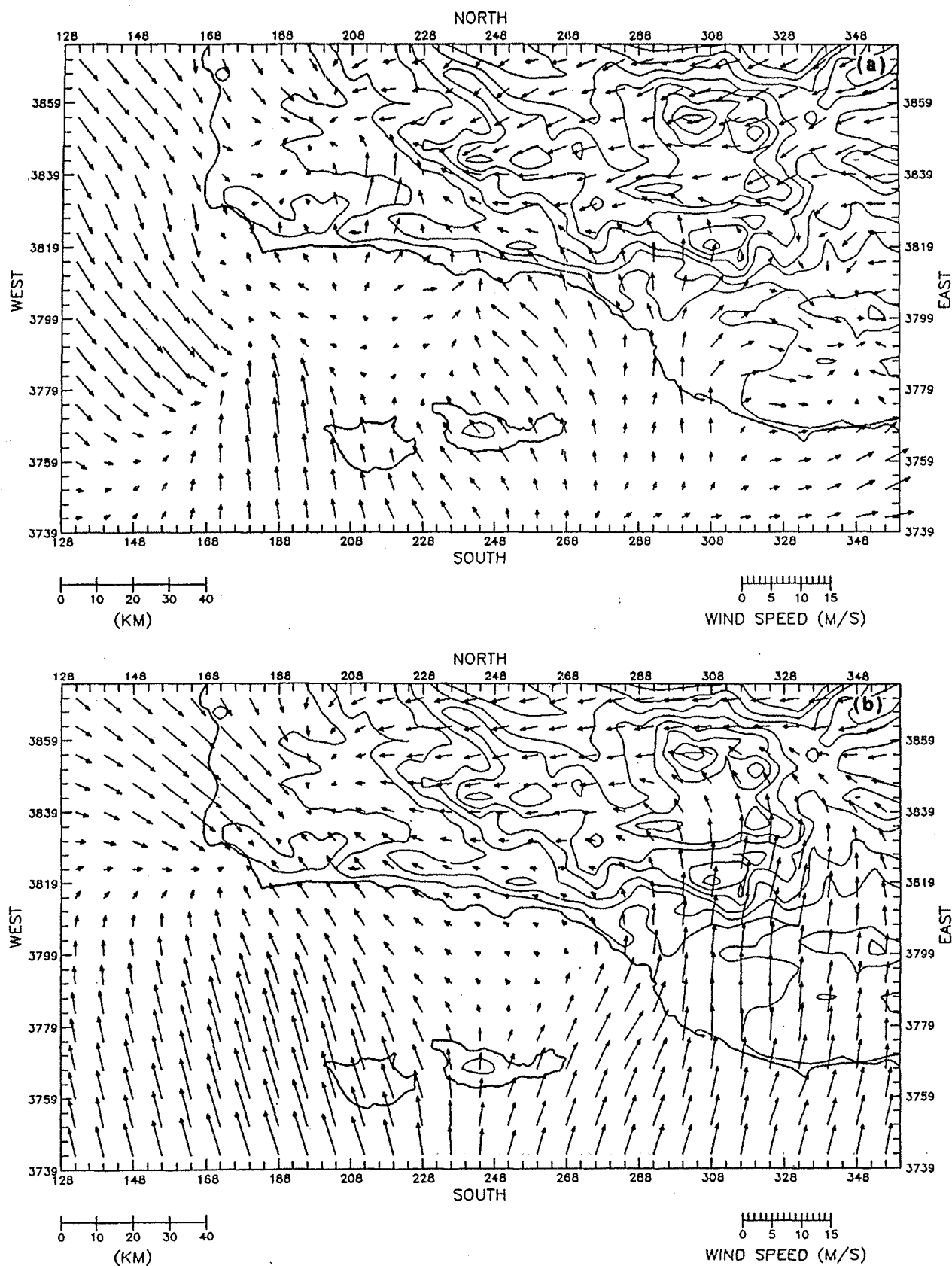


FIG. 12. As in Fig. 4, but for 24 September 1985.

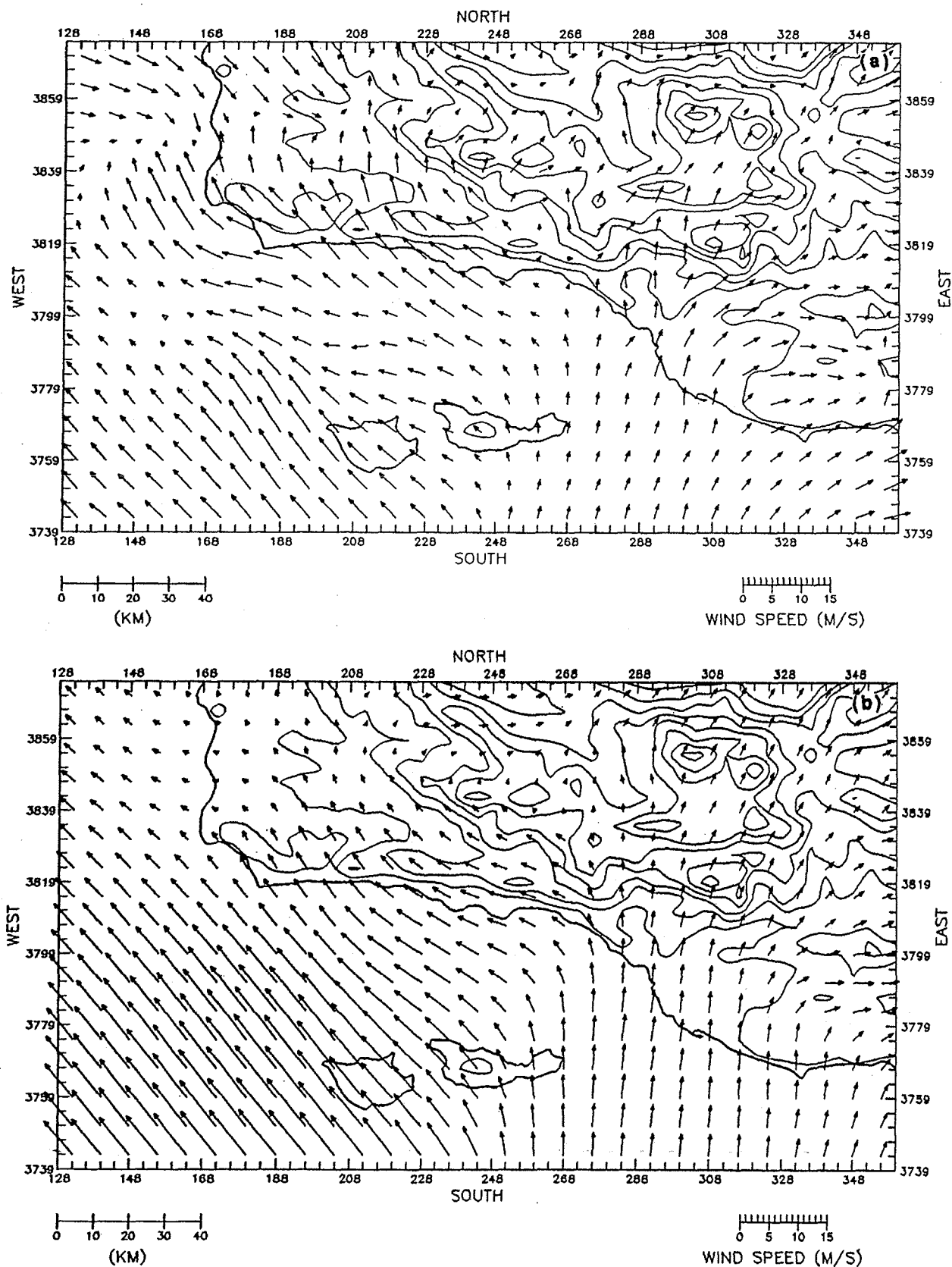


FIG. 13. As in Fig. 4, but for 25 September 1985.

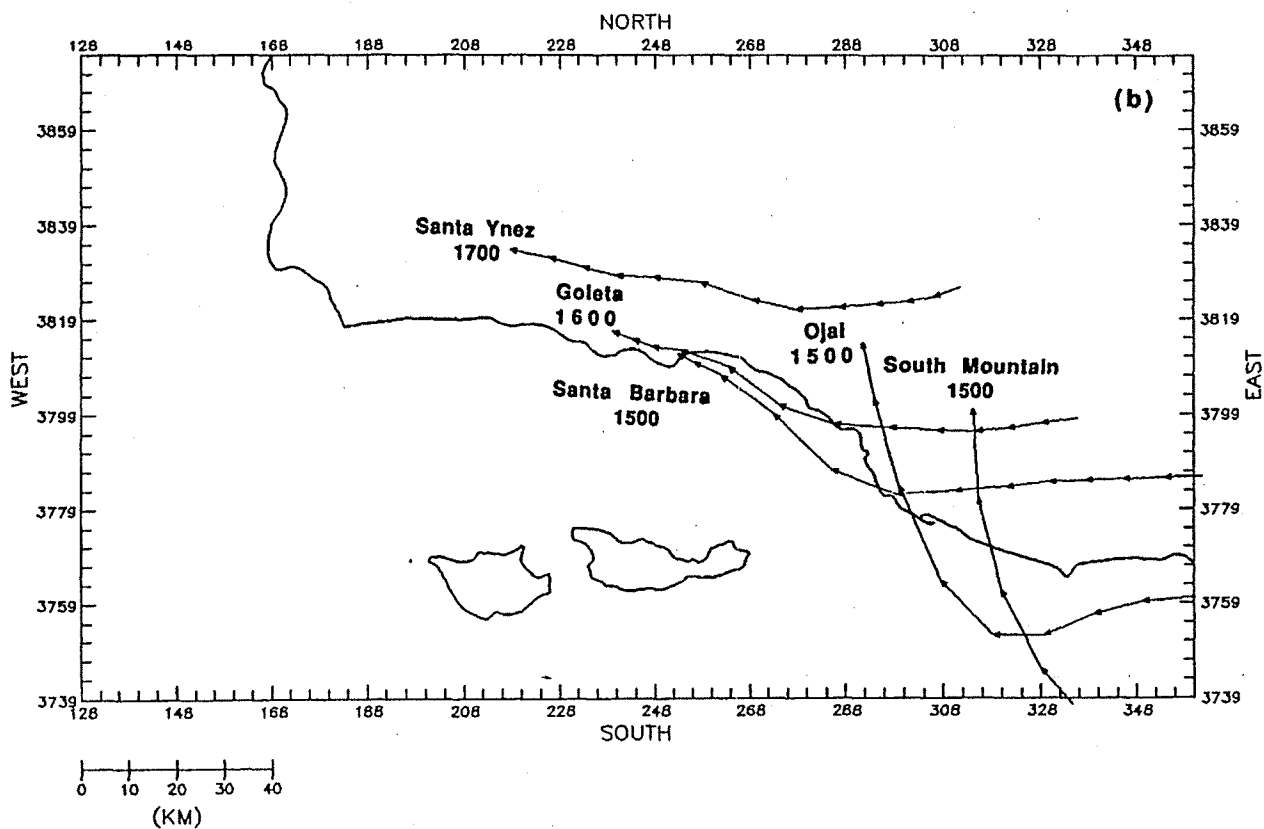
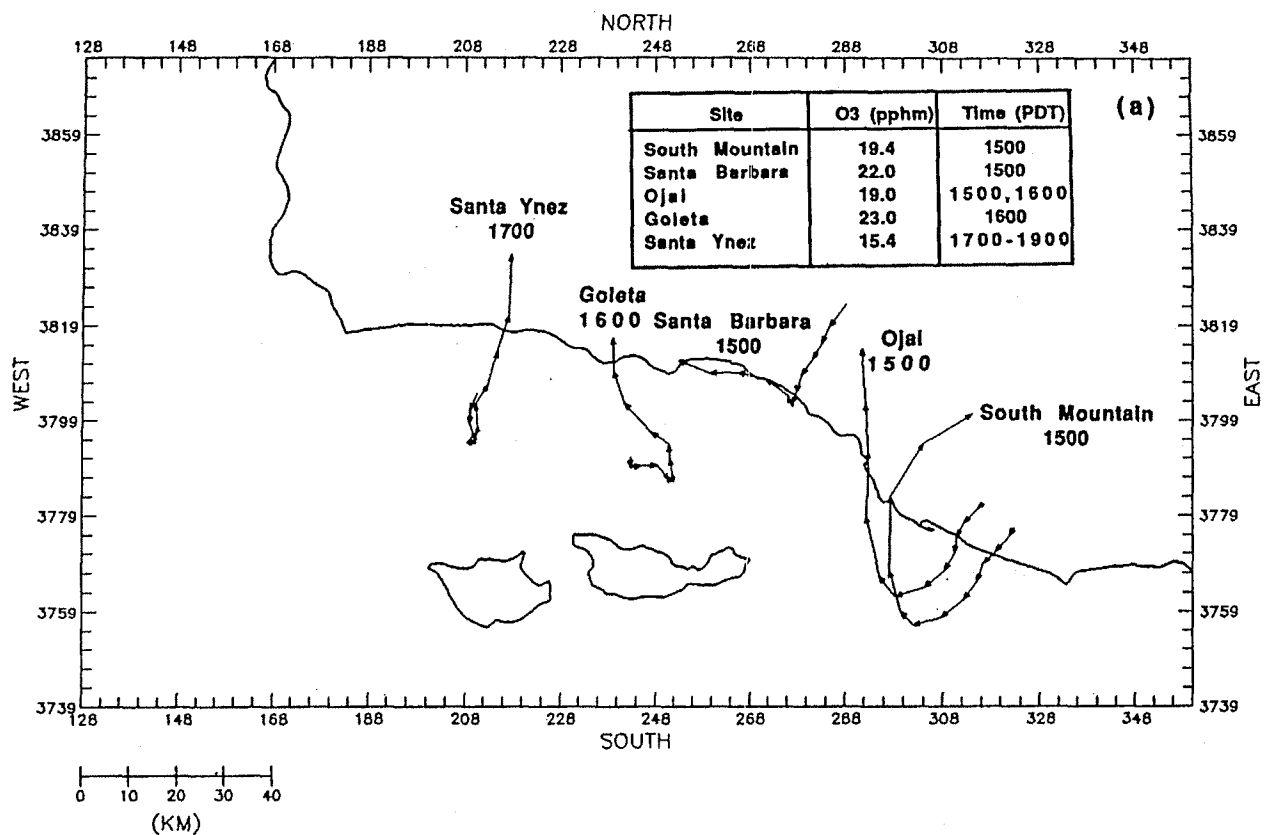


FIG. 14. As in Fig. 7, but for 24 September 1985.

low pressure system moved northwestward and high pressure over the western United States weakened.

2) MESOSCALE AIRFLOW PATTERNS

Diagnostic analyses of the airflow patterns for 2–4 October at the surface and 300 m AGL are presented in Figs. 15–18.

Mesoscale eddy development over the western channel is illustrated by the 0300 PDT 2 October surface analysis (Fig. 15). This eddy appears to have resulted from northeasterly flow near Point Conception, the persistent northwesterly flow over San Miguel Island, and southerly flow to the north of Santa Rosa Island. The variability of the observations indicate that this eddy is short lived. The remainder of the surface analysis is characterized by northeasterly flow inland, primarily easterly flow over the eastern channel, and offshore-directed flow along the coast. The morning airflow pattern at 300 m consisted of northerly flow along the eastern and western boundaries, northeasterly winds over much of Santa Barbara County, and south-easterly flow over the channel.

The sea breeze developed on this day by 1200 PDT at the surface and reached its maximum inland extent by 1500 PDT (Fig. 16a). The sea breeze mixed upward

to 300 m AGL by 1500 PDT (Fig. 16b). The retreat of the sea breeze occurred early on 2 October; by 1800 PDT winds along the coast were very light and by 2100 PDT winds were directed offshore.

On the morning of 3 October, surface winds in the southwestern portion of the domain were very weak. A weak cyclonic eddy was positioned to the west of Point Arguello and another is suggested to the north of Santa Rosa Island. At 300 m the wind gradually veered to the east during the night and by 0300 PDT winds at this level were easterly across the entire analysis domain. The westward extent of the easterly flow is significantly greater than on the other SCCAMP analysis days.

A low pressure system positioned off the coast of Baja California may account for the emergence of southerly flow on 3 and 4 October. At 1100 PDT on 3 October surface winds were quite variable but primarily southerly. By 1500 PDT (Fig. 17a) southerly flow had penetrated well inland, but spatial variability in the observed wind directions create an unusual pattern of convergence and divergence in the analysis of winds over the channel. The surface winds shifted to the southwest and a more typical sea-breeze regime dominated between 1800 and 2200 PDT. Easterly flow over the channel at the 300-m level became southerly

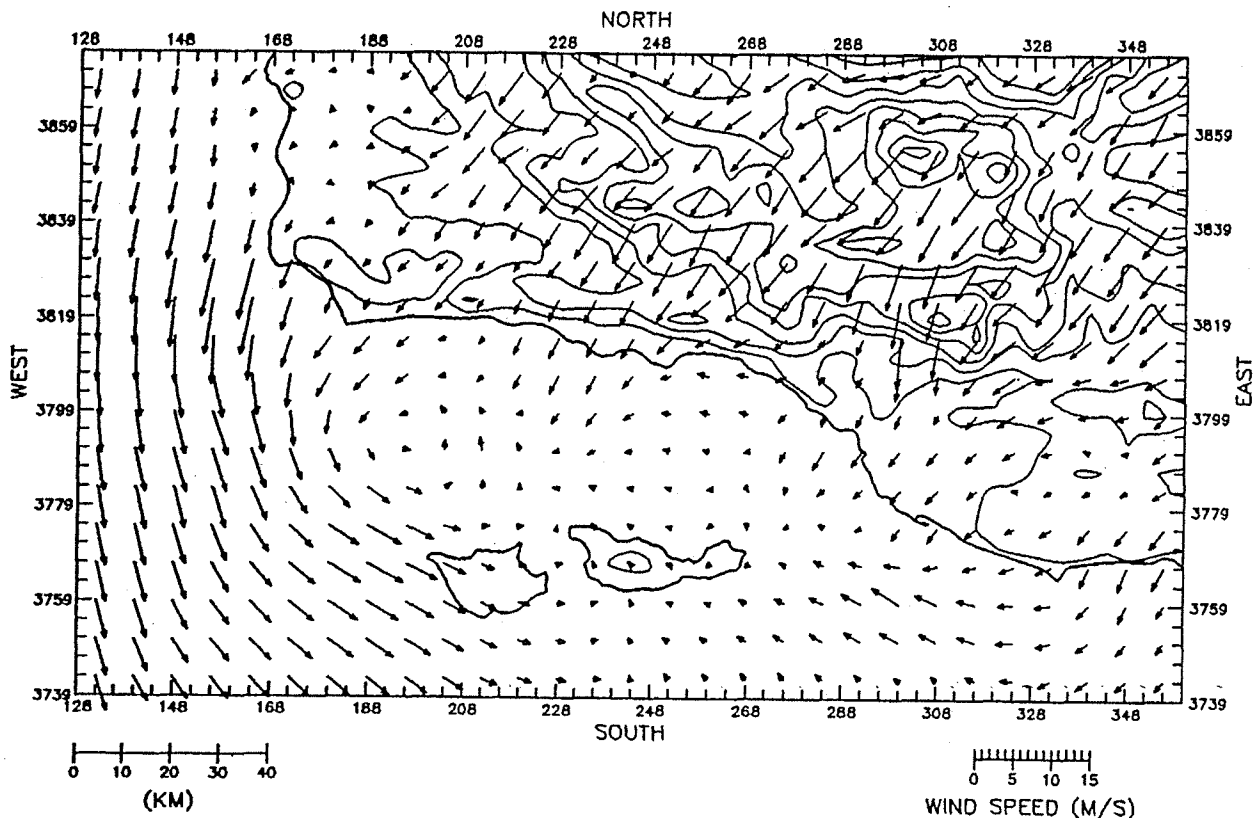


FIG. 15. Diagnostic wind field for 0300 PDT 2 October 1985 at 10 m AGL.

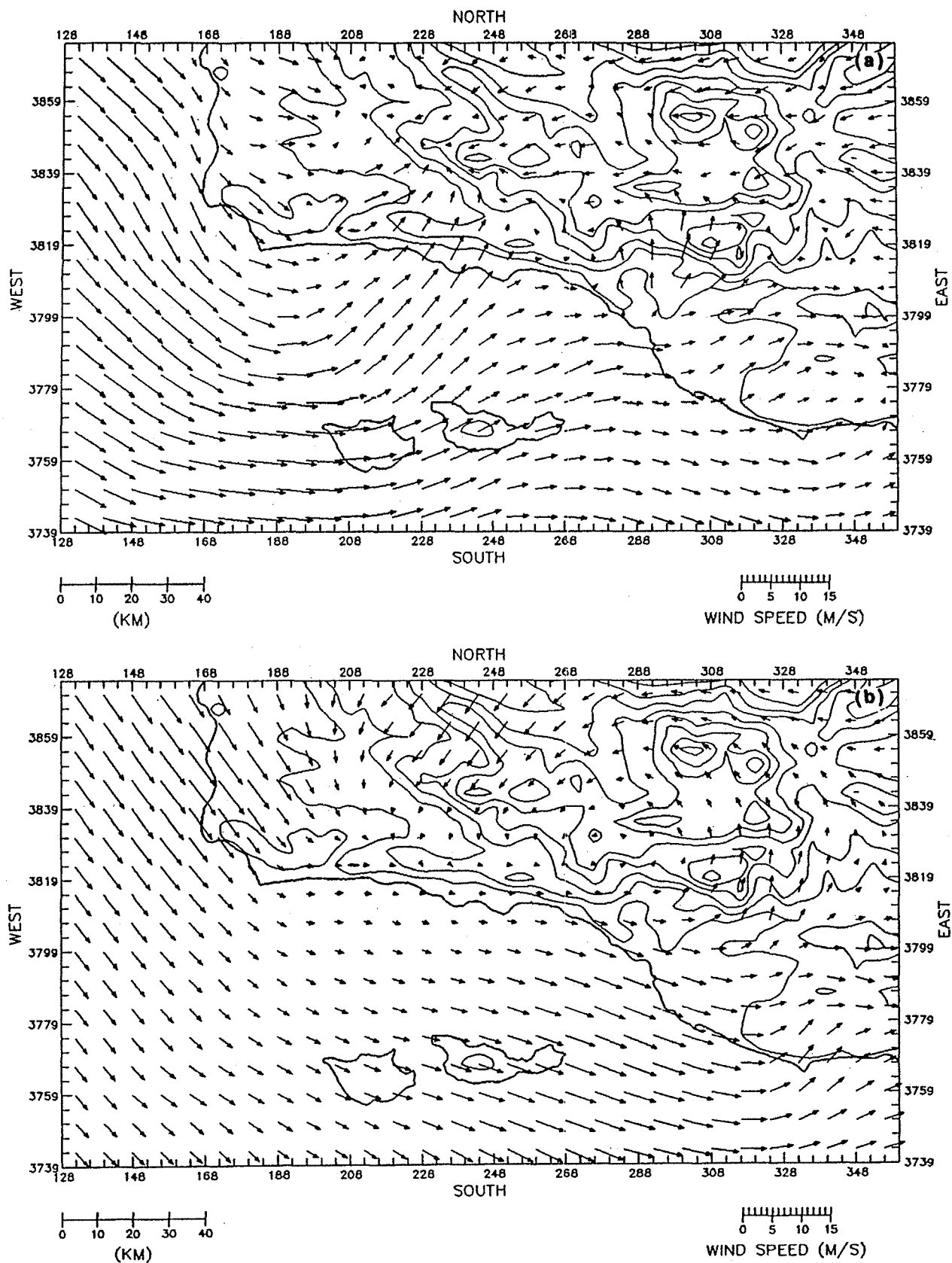


FIG. 16. As in Fig. 4, but for 2 October 1985.

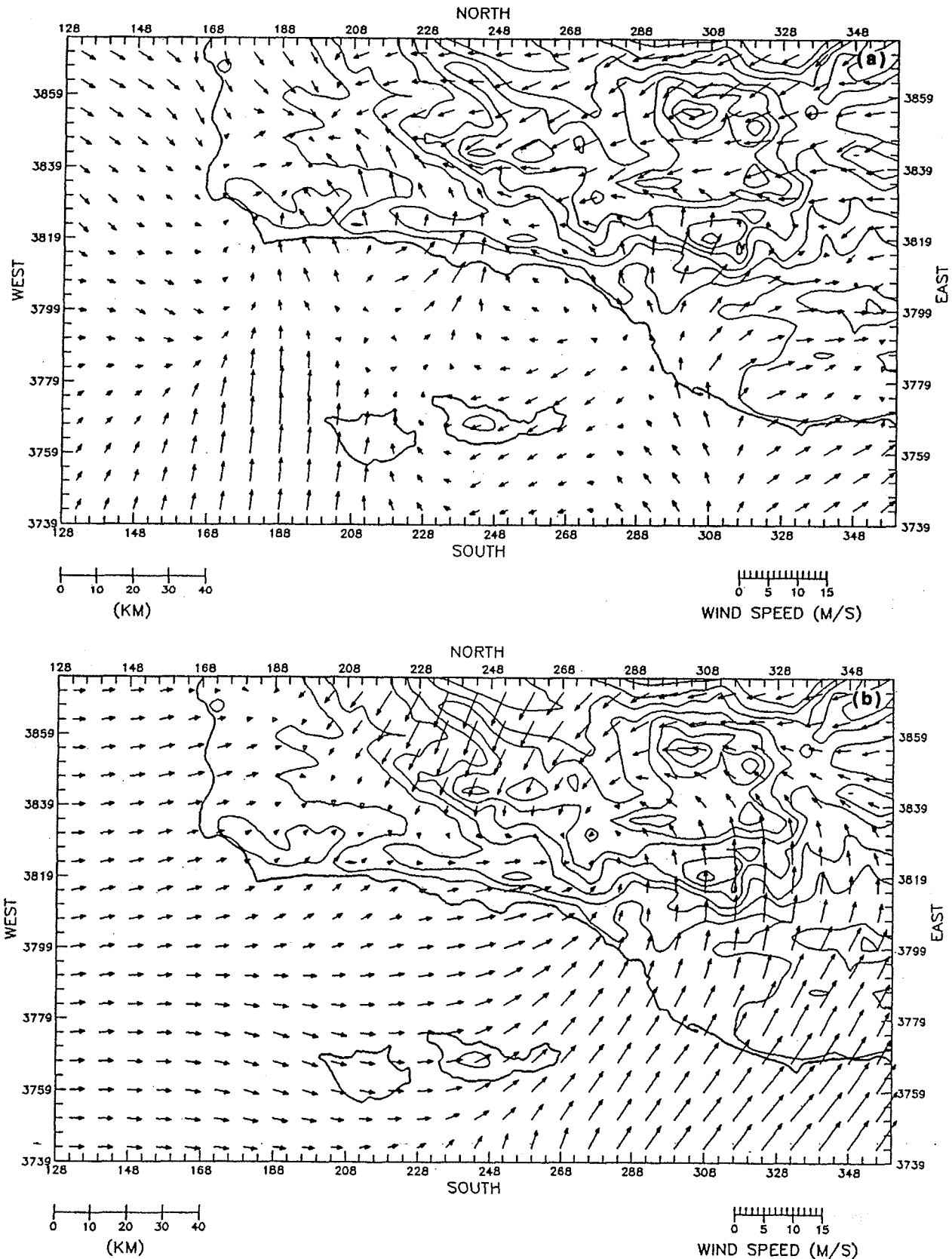


FIG. 17. As in Fig. 4, but for 3 October 1985.

by 1200 PDT and southwesterly by 1500 PDT (Fig. 17b). Winds at this level continued to veer until approximately 1800 PDT.

Airflow patterns on 4 October were similar to those on 3 October. The morning surface analyses suggest a combination of easterly flow and drainage flow over the channel. Southwesterly flow persisted only in the southwestern corner of the analysis domain. The 300-m AGL airflow was undergoing a transition from west to southeast, and the morning airflow was light and variable.

Surface winds over the channel developed a southerly component by 1100 PDT and continued to veer until 1500 PDT (Fig. 18a). Inland penetration of the onshore flow is indicated along the Santa Barbara coast and into Ventura County. Winds in the western part of the domain remained light. The flow over the channel at 300 m AGL (Fig. 18b) continued to veer becoming southerly at 1200 and westerly by 1800 PDT.

3) OZONE AIR-QUALITY SUMMARY

Ozone levels gradually increased between 2 and 3 October. The highest concentrations were observed along the coast and at offshore sites, peaking on 3 October with maximum concentrations of 20 pphm at San Miguel Island, platform Gina, and Anacapa Island. Concentrations gradually decreased on 4 October.

4) TRANSPORT PATTERNS

Backward particle paths for 3 October were calculated for Point Dume, platform Gina, Ellwood, Government Point, and San Miguel Island. Peak ozone concentrations occurred at Point Dume at 1400, platform Gina at 1600, San Miguel Island at 1700, and at Ellwood and Government Point at 1800 PDT.

In the eastern part of the domain (Point Dume and platform Gina) the surface-layer particle paths (Fig. 19a) illustrate the effects of offshore flow during the morning hours followed by southerly flow during the afternoon. Particles arriving at Ellwood and Government Point were positioned over the channel 12 h earlier and were advected westward, northwestward, and finally northeastward to the coast. At San Miguel Island, transport from south of the analysis domain is indicated.

Recirculation of pollutants over the channel (with net westward transport) is suggested by the 300-m AGL particle paths arriving at Ellwood, Government Point, and San Miguel Island in the late afternoon of 3 October (Fig. 19b). Possible transport from the south is indicated at platform Gina and Point Dume. Aircraft observations on the afternoon of 3 October detected a shallow polluted air mass over the channel. The particle paths indicate that sources both within and outside of the SCCAB may have contributed to this polluted air mass, which later affected coastal and offshore sites.

5. Summary

An analysis of the mesoscale airflow patterns in the south-central coast air basin (SCCAB) was performed using data collected during the 1985 South-Central Coast Cooperative Aerometric Monitoring Program (SCCCAMP). A large number of surface and upper-air monitoring sites were operated during the SCCCAMP and were primarily located within the coastal and offshore areas. The wind data were analyzed using a diagnostic wind model.

On most of the SCCCAMP intensive measurement days, a regionwide sea breeze develops that is channeled in a coast-parallel (generally west-east) direction by the coastal terrain. The extent of inland penetration of the sea breeze varies from day to day but usually encompasses the Oxnard plain and the Vandenberg area where coastal terrain obstacles are small. The sea-breeze layer can reach depths of 600 to 1000 m. On a number of the intensive measurement days, the development of the sea breeze is retarded or prevented by strong easterly synoptic forcing. A persistent feature of the afternoon wind field is the Gaviota eddy, a circulation that is formed by the persistent northwesterly flow around Point Arguello and upslope flow that develops along the Santa Barbara coast.

Nighttime airflow over the Santa Barbara Channel is generally characterized by propagation of easterly flow westward from the Point Dume area. This flow is opposed by persistent northwesterly flow at the western end of the channel. These opposing flows may contribute to the development of a midchannel eddy (Smith et al. 1983). Mechanisms that may be responsible for the development of this feature are discussed by Kessler and Douglas (1991), Mass and Albright (1989), and Wakimoto (1987). The nighttime airflow is also characterized by the development of offshore-directed downslope and drainage flows along the coast.

The complex mesoscale airflow patterns govern the transport of ozone and ozone precursor pollutants within the SCCAB and through its boundaries. Previous studies have indicated (see Hanna et al. 1991) that both recirculation of pollutants (by the diurnal land-breeze/sea-breeze cycle or eddies such as the midchannel eddy) and transport of pollutants (both at the surface and aloft) into the SCCAB from the SOCAB may contribute to high ozone concentrations in the region. Both mechanisms enhance the possibility that local emissions will produce exceedances of the NAAQS for ozone in the SCCAB. Interbasin transport pathways include 1) westward transport into Ventura County from the San Fernando Valley, 2) transport from the southeast through the inland valleys and along the coast, and 3) overwater transport westward from Los Angeles and then northward into the SCCAB (Hanna et al. 1991).

Backward particle paths indicate that both intrabasin and interbasin transport contributed to high ozone

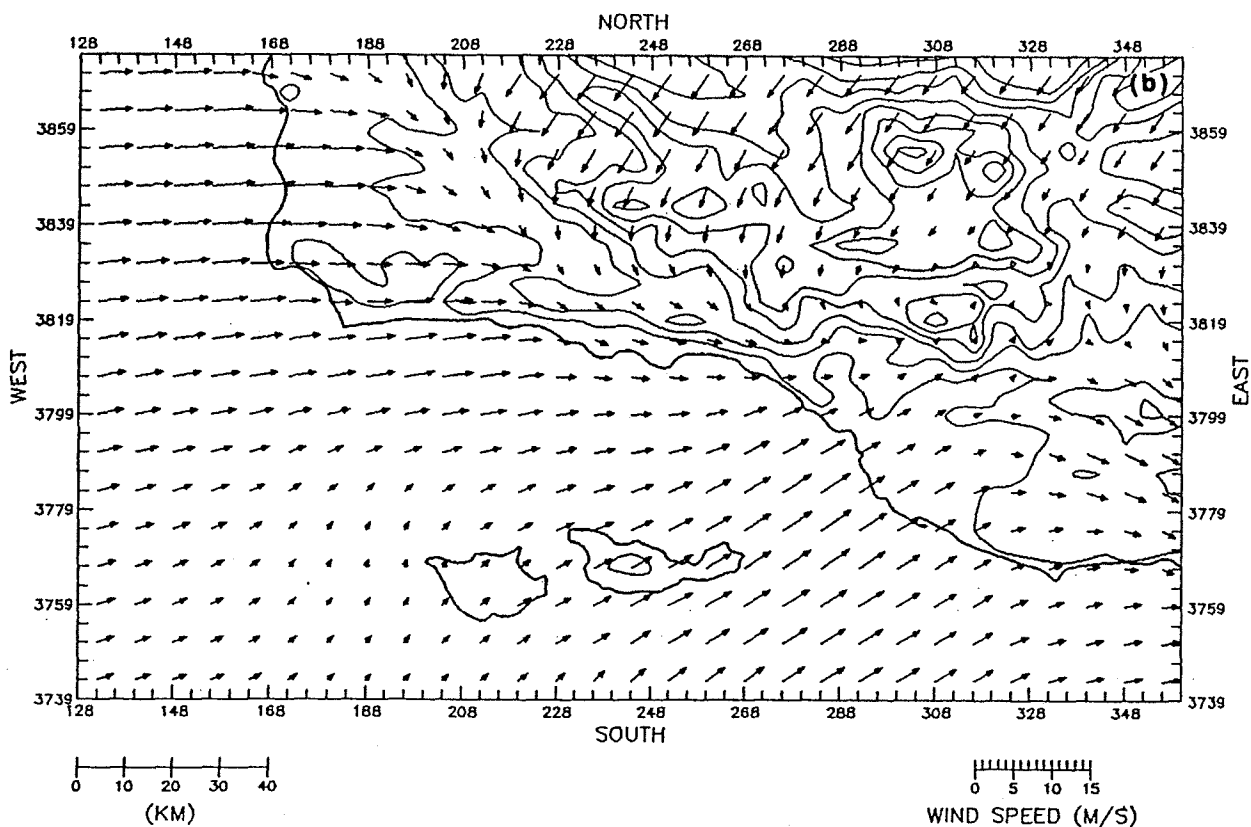
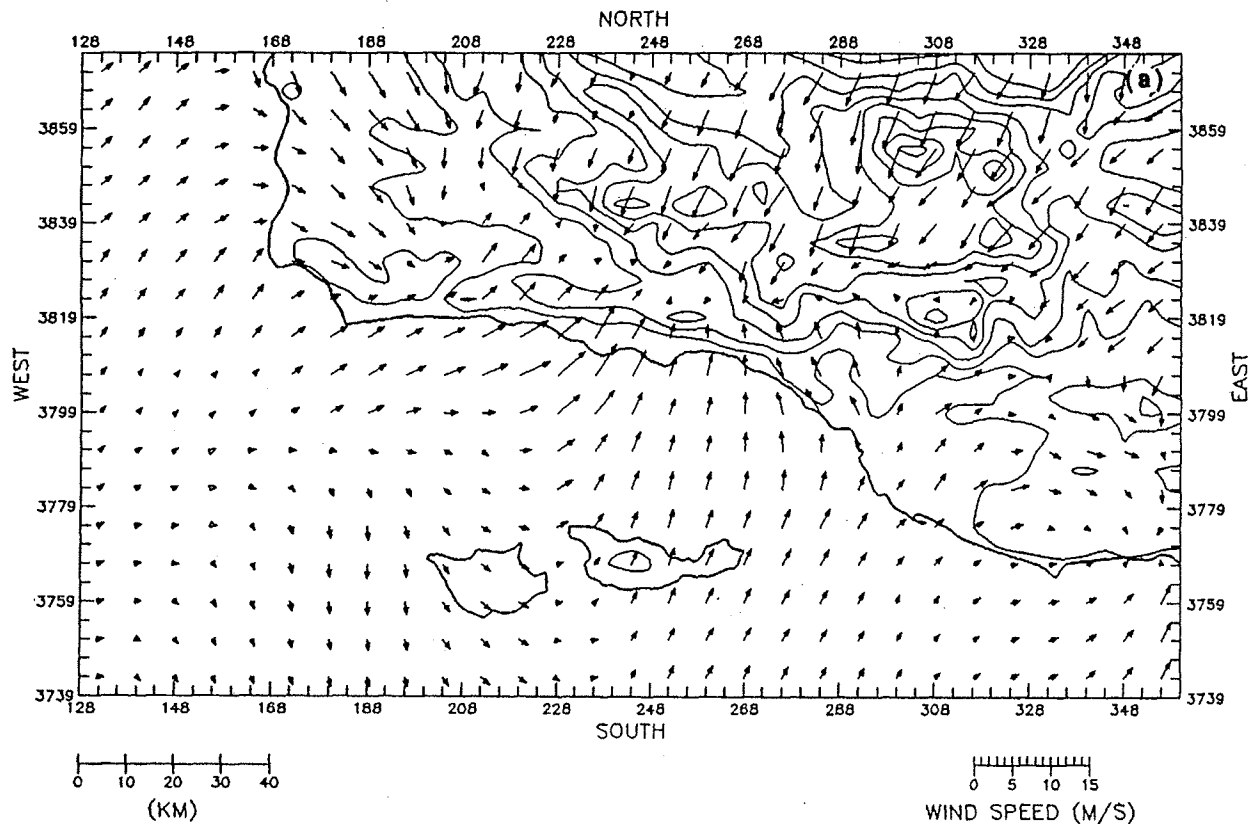


FIG. 18. As in Fig. 4, but for 4 October 1985.

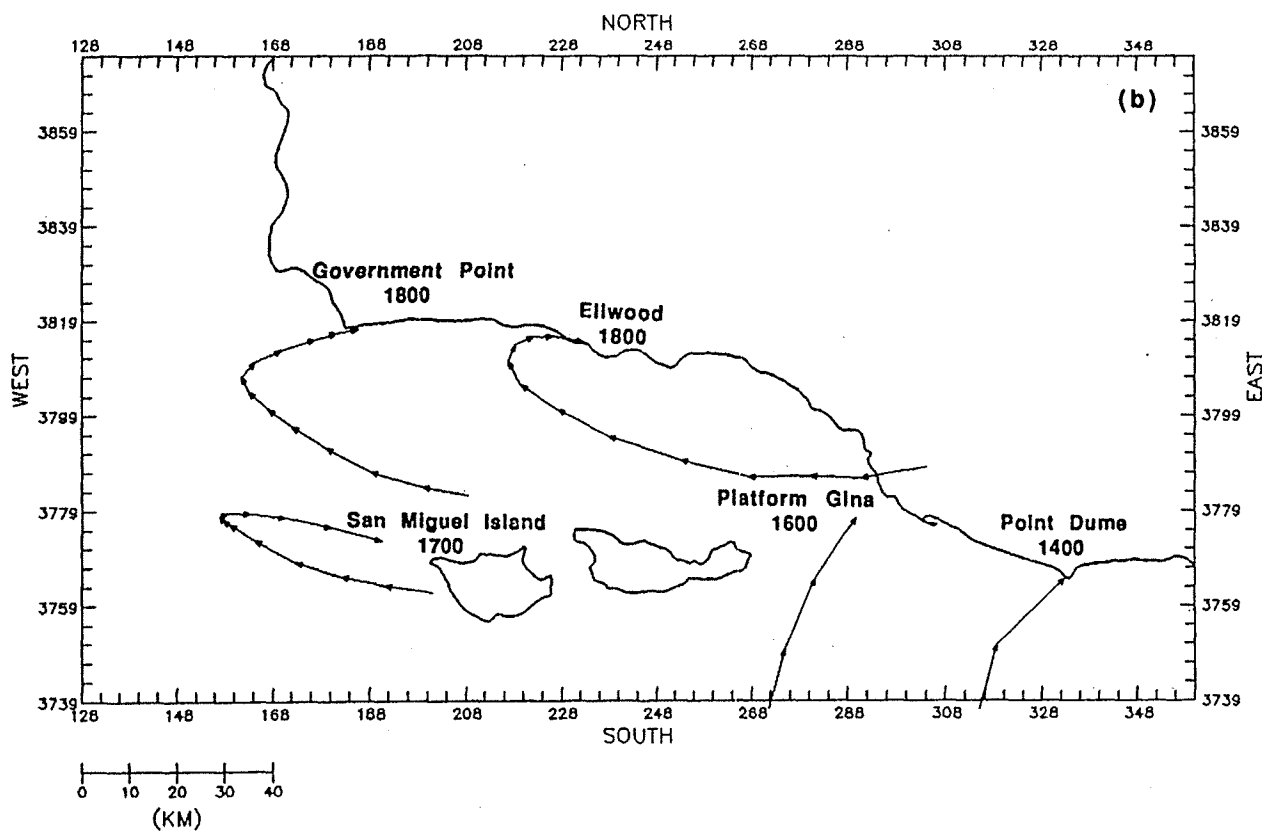
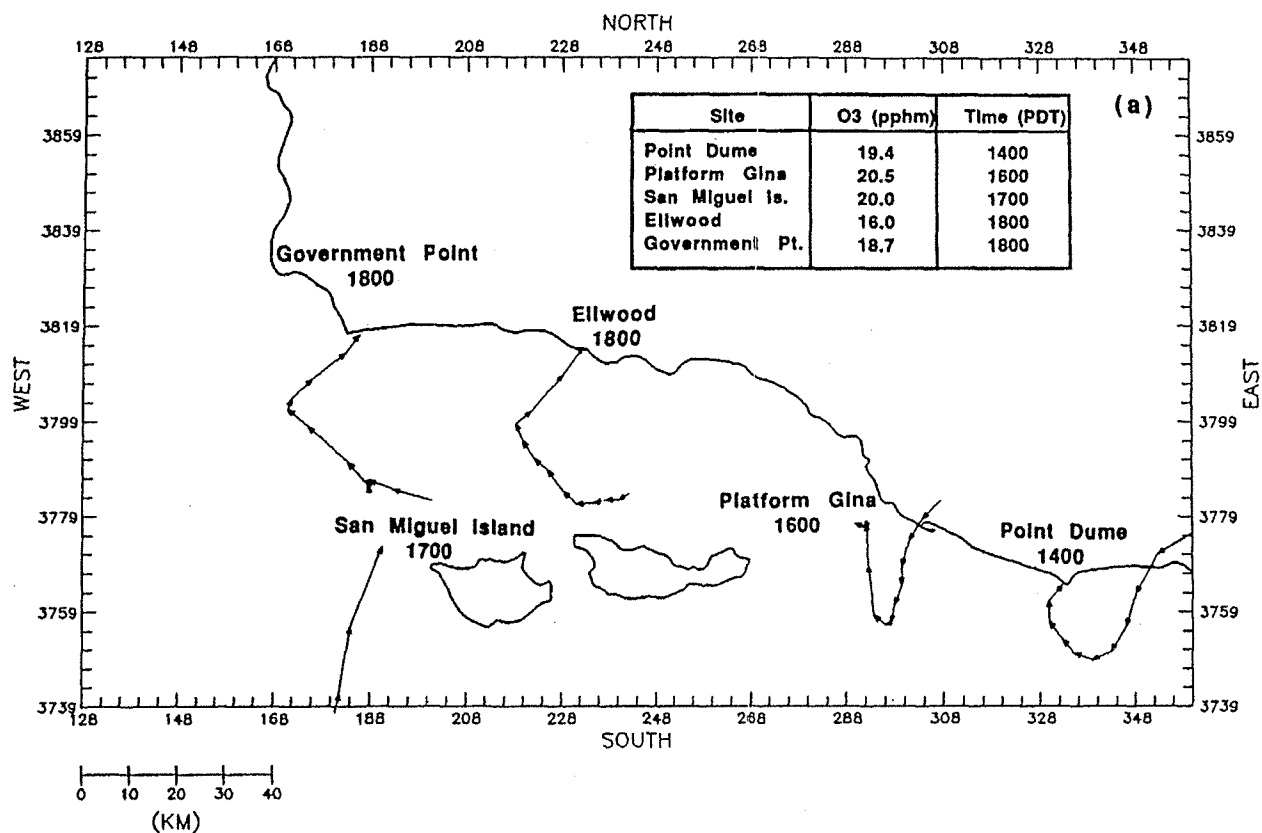


FIG. 19. As in Fig. 7, but for 3 October 1985.

concentrations within the SCCAB on the intensive study days. The surface-layer particle paths for 13 September indicate possible recirculation of pollutants by the land-breeze/sea-breeze cycle while the 300-m AGL particle paths indicate overwater transport from the southeast. On 24 September, the surface-layer particle paths indicate possible recirculation of pollutants and contribution from offshore sources, while the upper-level particle paths indicate transport westward from the San Fernando Valley into Ventura and Santa Barbara counties and overwater transport from Los Angeles into Ventura County. The surface-layer particle paths for 3 October indicate possible recirculation as well as transport from the south, while at 300 m AGL transport from the south (Los Angeles) is indicated in the eastern part of the domain and westward transport while some recirculation is indicated in the western part of the domain. In contrast, particle paths for 21 September (a nonexceedance day) indicate transport of clean air into the SCCAB from the north and from over the ocean and the channel.

Acknowledgments. This work was sponsored by the U.S. Department of the Interior Minerals Management Service (MMS) under Contract 14-12-0001-30329. We gratefully acknowledge the SCCCAMP Technical Advisory Committee and especially Mr. Thomas Chico (MMS Technical Representative) for their contributions to the project.

REFERENCES

- Dabberdt, W. F., and W. Viezee, 1987: South Central Coast Cooperative Aerometric Monitoring Program (SCCCAMP). *Bull. Amer. Meteor. Soc.*, **68**, 1098–1110.
- Hanna, S. R., D. G. Strimaitis, J. S. Seire, G. E. Moore and R. C. Kessler, 1991: Overview of results of analysis of data from the South-Central Coast Cooperative Aerometric Monitoring Program (SCCCAMP-1985). *J. Appl. Meteor.*, **30**, 511–533.
- Kessler, R. C., and S. G. Douglas, 1991: A numerical simulation of mesoscale eddy development over the Santa Barbara Channel. *J. Appl. Meteor.*, **30**, 633–651.
- , L. L. Schultman, S. G. Douglas and E. L. Hovind, 1988: Analysis of wind fields for the SCCCAMP 1985 intensive measurement periods. Rep. To United States Dept. of Interior, Contract No. 14-12-0001-3029, 178 pp. [Available from SRI International, Menlo Park, CA.]
- Mass, C. F., and M. D. Albright, 1989: Origin of the Catalina eddy. *Mon. Wea. Rev.*, **117**, 2406–2436.
- Ross, D. G., and I. Smith, 1986: Diagnostic wind field modeling for complex terrain—testing and evaluation. 93 pp. [Available from the Centre for Applied Mathematical Modeling, Chisolm Institute of Technology, Melbourne, Australia.]
- Smith, T. B., W. D. Saunders and F. H. Shair, 1983: Analysis of Santa Barbara oxidant study. Final Rep. to California Air Resources Board, Agreement A2-086-32, 236 pp. [Available from Meteorology Research, Inc., Altadena, CA.]
- Viezee, W., R. M. Endlich and J. Kealoha, 1987: Auxiliary data volume for the South Central Coast Cooperative Aerometric Monitoring Program. MMS-87-0087, 316 pp. [Available from USDO, MMS, Pacific OCS Region, Los Angeles, CA.]
- Wakimoto, R. M., 1987: The Catalina eddy and its effect on pollution over southern California. *Mon. Wea. Rev.*, **114**, 1330–1339.

UNION OF CONCERNED SCIENTISTS

Citizens and Scientists for Environmental Solutions

www.ucsusa.org

Clean California


Mail this to a friend

Climate Change Campaign

California Global Warming Impacts and Solutions

2/2006

How Will Global Warming Impact California?

IPCC Emissions Scenarios	Summary of Projected Global Warming Impacts (2070-2099, as compared to 1961-1990)	State-wide Temperature Rise
<p>Higher Emissions: Rapid, fossil-fuel intensive growth</p> 	<ul style="list-style-type: none"> ● 90% loss in Sierra snow pack ● 22-30 inches of sea level rise ● 3-4 times as many heatwave days in major urban centers ● 2.5 times the number critically dry years ● 4-6 times as many heat-related deaths in major urban centers ● 20% increase in electricity demand ● Increase in days meteorologically conducive to ozone formation 	<p>Higher Warming Range: 8-10.4 °F</p>
<p>Medium-High Emissions: Primarily fossil-fuel dependent growth with some green technology</p>	<ul style="list-style-type: none"> ● 70- 80 % loss in Sierra snow pack ● 14-22 inches of sea level rise ● 2.5-4 times as many heatwave days in major urban centers ● 2-6 times as many heat-related deaths for major urban centers ● 75-85% increase in days meteorologically conducive to ozone 	<p>Medium Warming Range: 5.5-7.9 °F</p>

Lower Emissions:
Shift to service & information economy with lots of green technology

- formation
- 2-2.5 times the number critically dry years
- 11% increase in electricity demand
- 30% decrease in forest yields (pine)
- 55% increase in the expected risk of large wildfires
- 30-60 % loss in Sierra snow pack
- 6-14 inches of sea level rise
- 2-2.5 times as many heatwave days in major urban centers
- 2-3 times as many heat-related deaths for major urban centers
- 25-35% increase in days meteorologically conducive to ozone formation
- Up to 1-1.5 times the number critically dry years
- 3-6 % increase in electricity demand
- 7-14% decrease in forest yields (pine)
- 10-35% increase in the risk of large wildfires

Lower Warming
Range:
3.0-5.4 °F

Source: Cayan, D., Luers, A., Hanemann, M., Franco, G. and Croes, B. 2006. Climate Change Scenarios for California: an Overview. California Energy Commission PIER working paper.

The more global warming emissions are reduced, the less severe the impacts will be.

California has a choice: continue contributing to an alarming rate of global warming by emitting large quantities of global warming pollutants from its cars, electricity plants, and factories, or lead the nation and the world in slowing global warming by making significant cuts in emissions.

How much would global warming emissions have

to be reduced to ensure that we stay in or below the lower warming range?

If the industrialized world were to follow California's lead of reducing emissions 80 percent below 1990 levels by 2050 and the industrializing nations followed thereafter, global emissions would remain in or below the lower emissions scenario, thus increasing the likelihood that California and the world would be on track to avoid the more severe impacts.

California's Responsibility to Act

California is the 12th largest source of global warming emissions in the world, exceeding most entire countries. California has a responsibility to reduce its global warming emissions, and by doing so can lead the United States, and the world, in developing the innovative policies and technologies needed to avoid the most dangerous impacts of global warming. Two independent teams of the state's top economists calculate that significantly reducing global warming emissions can boost the state's economy by billions of dollars and create tens of thousands of jobs in the coming decades.

Global Warming Emission Reduction Targets

In June 2005 Governor Schwarzenegger signed an Executive Order committing the state to the following targets for reducing global warming emissions:

- By 2010, California emissions will be reduced to 2000 levels, or by 11 percent
- By 2020, California emissions will be reduced to 1990 levels, or by 25 percent
- By 2050, California emissions will be reduced to 80 percent below 1990 levels

Policy Recommendations for 2006

A strong, enforceable cap on global warming emissions will be needed to achieve the reductions called for in the governor's targets. The governor and legislature should work together to codify the governor's targets and create an enforceable and declining cap on global warming emissions for the sectors of the economy that comprise the largest

emitters. In order for a cap to work, verifiable mandatory reporting of global warming emissions for those sectors will be required.

Sector-specific regulatory programs offer important opportunities for reducing emissions as well. Implementing aggressive renewable energy and energy efficiency policies for all electric providers in the state is essential. As the transportation sector will continue to be the largest source of global warming emissions in California for the foreseeable future, additional measures will be needed beyond the landmark emissions standards for vehicles now in place. For example, a self-financing program of emission-based discounts and surcharges on new cars will help consumers and families purchase cleaner new cars and encourage auto manufacturers to offer cleaner, more efficient cars to California drivers.

Page Last Revised: 03/02/06

with a lattice that has an in-plane orientational epitaxy with the underlying mica lattice. The only reason x-ray analysis can be carried out on these structures is because we are able to signal average over a large collection of prisms that are aligned with one another and epitaxially arranged on the mica support.

This approach to controlling and monitoring the kinetics of crystal growth can be used to study environment-imposed changes in crystal morphology (28). Subtle changes in temperature markedly affect the growth of the crystals and the observed morphology of the crystals ultimately formed. Indeed, when the temperature is increased to 35°C, cubic-shaped features emerge at the edges of the prisms while scanning the crystals that were preformed at lower temperature with the PLH-coated AFM tip (Fig. 4). This morphological change is very reproducible and always was induced at the corners or edges of the starting triangular crystals.

This study provides an approach for site-specifically initiating crystal growth on the nanometer-length scale in a way that allows one to monitor growth from crystal seed to more mature structures as a function of environmental conditions (fig. S5). The size of the smallest crystal observed and studied in these experiments (d in Fig. 1) is five orders of magnitude smaller than what could be studied by single-crystal XRD techniques, allowing one to observe morphological changes that would typically go undetected in an x-ray study that

focuses on larger structures. Finally, growing crystals of macromolecules is not a trivial process. DPN is now a massively parallel tool (16, 29, 30), suggesting that this study may open the door for creating combinatorial approaches to identifying the proper conditions to initiate a particular type of crystal growth for a given set of target molecules.

References and Notes

1. E. M. Landau, M. Levanon, L. Leiserowitz, M. Lahav, J. Sagiv, *Nature* **318**, 353 (1985).
2. Y. Yin et al., *Science* **304**, 711 (2004).
3. S. Mann, G. A. Ozin, *Nature* **382**, 313 (1996).
4. J. L. Fransaer, R. M. Penner, *J. Phys. Chem. B* **103**, 7643 (1999).
5. S. A. Empedocles, M. G. Bawendi, *Science* **278**, 2114 (1997).
6. J. J. Pluth et al., *Proc. Natl. Acad. Sci. U.S.A.* **94**, 12263 (1997).
7. A. C. Hillier, M. D. Ward, *Science* **263**, 1261 (1994).
8. M. D. Ward, *Chem. Rev.* **101**, 1697 (2001).
9. D. E. Hooks, C. M. Yip, M. D. Ward, *J. Phys. Chem. B* **102**, 9958 (1998).
10. T. A. Land, A. J. Malkin, Y. G. Kuznetsov, A. McPherson, J. J. De Yoreo, *Phys. Rev. Lett.* **75**, 2774 (1995).
11. H. H. Teng, P. M. Dove, C. A. Orme, J. J. De Yoreo, *Science* **282**, 724 (1998).
12. J. K. Hobbs, M. J. Miles, *Macromolecules* **34**, 353 (2001).
13. N. Sanz, J. K. Hobbs, M. J. Miles, *Langmuir* **20**, 5989 (2004).
14. J. K. H. Hörber, M. J. Miles, *Science* **302**, 1002 (2003).
15. R. D. Piner, J. Zhu, F. Xu, S. Hong, C. A. Mirkin, *Science* **283**, 661 (1999).
16. D. S. Ginger, H. Zhang, C. A. Mirkin, *Angew. Chem. Int. Ed. Engl.* **43**, 30 (2004).
17. B. W. Maynor, J. Li, C. Lu, J. Liu, *J. Am. Chem. Soc.* **126**, 6409 (2004).
18. R. J. Barsotti, M. S. O'Connell, F. Stellacci, *Langmuir* **20**, 4795 (2004).
19. G. Agarwal, L. A. Sowards, R. R. Naik, M. O. Stone, *J. Am. Chem. Soc.* **125**, 580 (2003).
20. B. S. Jacobson, D. Branton, *Science* **195**, 302 (1977).
21. W. Dzwolak, R. Ravindra, C. Nicolini, R. Jansen, R. Winter, *J. Am. Chem. Soc.* **126**, 3762 (2004).
22. B. Ratner, V. V. Tsukruk, *Scanning Probe Microscopy in Polymers* (ACS Symposium Series, American Chemical Society, Washington, DC, 1998).
23. The orientation is not related to the tip scanning direction. Change of the orientation of the mica substrate does not change the growth of the prisms or their orientation with respect to each other and the mica.
24. X. Liu et al., data not shown.
25. R. Kern, in *Crystal Growth in Science and Technology*, H. Arend, J. Hulliger, Eds. (Plenum Press, New York, 1989), pp. 143–165.
26. Materials and methods are available as supporting material on Science Online.
27. D. A. Walko et al., *AIP Conf. Proc.* **705**, 1166 (2004).
28. W. C. McCrone, in *Physics and Chemistry of Organic Solid State*, D. Fox, M. M. Labes, A. Weissberger, Eds. (Interscience, New York, 1965), pp. 726–767.
29. S. Hong, C. A. Mirkin, *Science* **288**, 1808 (2000).
30. D. Bullen, S. W. Chung, X. Wang, J. Zou, C. A. Mirkin, *Appl. Phys. Lett.* **84**, 789 (2004).
31. Supported by the Nanoscale Science and Engineering Initiative of the NSF under NSF Award No. EEC-0118025, the NIH through Award No. GM62109-02, and a Director's Pioneer Award to C.A.M., the Institute for BioNanotechnology in Medicine, Baxter Healthcare Corp, and the Air Force Office of Scientific Research (AFOSR) through a Multidisciplinary University Research Initiative (MURI) Award.

Supporting Online Material

www.sciencemag.org/cgi/content/full/307/5716/1763/DC1

Materials and Methods

Figs. S1 to S5

Table S1

References

6 January 2005; accepted 3 February 2005
10.1126/science.1109487

The Climate Change Commitment

T. M. L. Wigley

Even if atmospheric composition were fixed today, global-mean temperature and sea level rise would continue due to oceanic thermal inertia. These constant-composition (CC) commitments and their uncertainties are quantified. Constant-emissions (CE) commitments are also considered. The CC warming commitment could exceed 1°C. The CE warming commitment is 2° to 6°C by the year 2400. For sea level rise, the CC commitment is 10 centimeters per century (extreme range approximately 1 to 30 centimeters per century) and the CE commitment is 25 centimeters per century (7 to 50 centimeters per century). Avoiding these changes requires, eventually, a reduction in emissions to substantially below present levels. For sea level rise, a substantial long-term commitment may be impossible to avoid.

Oceanic thermal inertia causes climate change to lag behind any changes in external forcing and causes the response to be damped relative to the asymptotic equilibrium response (1–3). Because of this lag or damping effect, and because of the changes in atmospheric composition (and radiative forcing) that have already occurred, the climate system will continue to change for many decades (centuries for sea level) even in the absence of future changes in

atmospheric composition. For global-mean temperature, this is referred to as the “unrealized warming” (2), “residual warming” (4), or “committed warming” (5). Here, I use the term “warming commitment” or, to include sea level rise (6, 7), “climate change commitment.”

The assumption of constant atmospheric composition on which the warming commitment idea is based is clearly unrealistic, even as an extreme case of what might happen in the future. An alternative indicator of the commitment to climate change is to assume that the emissions (rather than concentrations)

of radiatively important species will remain constant. This Report investigates the constant-composition (CC) warming and sea level commitments, the constant-emissions (CE) commitments, and the uncertainties in each. Uncertainties arise from uncertainties in the climate sensitivity (2, 4), the rate of ocean heat uptake (2), the magnitude of past forcing, and the ice melt contribution to sea level change.

The usual (or “equilibrium”) CC warming commitment at time t is the difference between the equilibrium warming for forcing at this time (ΔT_e) and the corresponding realized warming (ΔT_r), $\Delta T_e - \Delta T_r$. This is related to the “radiation-imbalance” concept (8, 9). If ΔQ is the forcing to date, and if ΔQ_r is the forcing that gives an equilibrium warming of ΔT_r , then the radiation imbalance is $\Delta Q - \Delta Q_r$ [$\Delta Q - \Delta Q_r$ is approximately equal to the flux of heat into the ocean (9)]. Hence

$$\Delta T_e - \Delta T_r = (\Delta Q - \Delta Q_r)(\Delta T_2 \times / \Delta Q_2 \times)$$

where $\Delta Q_2 \times$ is the radiative forcing for a CO₂ doubling (about 3.7 W/m²) and $\Delta T_2 \times$ is the corresponding equilibrium global-mean warming. A central estimate of ΔQ (accounting for both natural and anthropogenic forcings) is about 1.7 W/m², whereas ΔT_r is about

National Center for Atmospheric Research, Boulder, CO 80307, USA. E-mail: wigley@cgd.ucar.edu

0.7°C. Given $\Delta T_{2\times} = 2.6^\circ\text{C}$ (10), a central value for the current equilibrium warming commitment is about 0.5°C, with a corresponding radiation-imbalance estimate of 0.7 W/m². These results are in accord with other estimates in the literature, but uncertainties are large.

Because it would take an infinite time for the unrealized warming to appear, a more useful definition makes the unrealized warming a time-dependent quantity, namely, the evolving changes in global-mean temperature that would result if atmospheric composition were kept constant at its present state (4). This is the definition I use here. Temperatures under this new definition tend asymptotically to the previous equilibrium commitment definition. The new definition can be applied equally to the CC and CE commitments and can be used for both temperature and sea level.

To quantify the changes in global-mean temperature and sea level that would occur if either atmospheric composition or the emissions of radiatively important gases were kept constant at today's levels (the year 2000 is used to define "today"), I used the simple coupled gas-cycle/climate model MAGICC (10–12). MAGICC has been calibrated against a range of coupled atmosphere/ocean general-circulation models (13, 14) and was used in the Intergovernmental Panel on Climate Change (IPCC) Third Assessment Report (TAR) and earlier IPCC reports to produce the standard projections of global-mean temperature and sea level change. For access to MAGICC, see (15).

For sea level rise commitments, a change has been made in the way the melt contribution from land-based glaciers and Small Ice Caps (GSICs) is calculated. In the TAR, the GSIC formula was only meant to be applied through the year 2100 (I project to the year 2400 here). Because of an empirical area-correction term used in the TAR (16), GSIC results are unrealistic beyond 2100, and the correction term imposes an artificial melt maximum (17). The modified formulation (17) matches the TAR results well through the year 2100 and then tends asymptotically to the initially available GSIC ice mass (taken as 40-cm sea level equivalent).

The other TAR sea level rise terms are (16) thermal expansion (a direct output of the climate model), mass-balance changes for the Greenland and Antarctic ice sheets, long-time-scale changes in these ice masses due to past climate change, deposition of sediments on the ocean floor, and runoff from the thawing of permafrost. In the TAR formulation, the last three components (referred to here as "unforced contributions") are independent of past forcings. To quantify nonexpansion uncertainties, I used methods employed in the TAR.

For the CC and CE temperature commitments, the primary sources of uncertainty are past radiative forcing, the climate sensitivity, and the rate of ocean heat uptake. For past

forcing, I considered the effect of natural forcings from solar irradiance changes (18) and volcanic eruptions (19), and uncertainties in aerosol forcing. For climate sensitivity, I used a central value of $\Delta T_{2\times} = 2.6^\circ\text{C}$ and a range of 1.5° to 4.5°C, approximately equal to the 90% confidence interval (CI) (10). For ocean mixing, I used vertical diffusivities (K_z) of 1.3, 2.3, and 4.1 cm²/s, also representing the 90% CI and median values (10).

A breakdown of the natural and anthropogenic components of the CC commitment, together with uncertainties arising from ocean mixing (K_z) uncertainties, is given in table S1. Past natural forcing (inclusion of which is the default case here) has a marked effect. The natural forcing component is surprisingly large, 64% of the total commitment in 2050, reducing to 52% by 2400. The effect of ocean mixing uncertainties is small, at most 7%.

Overall results and uncertainties associated with aerosol forcing and the climate sensitivity are shown in Fig. 1 (CC case) and Fig. 2 (CE case). Aerosol forcing is characterized by the forcing in 1990. The central values (and uncertainty ranges) are those used for global-mean warming projections in the TAR

(10, 13): -0.4 W/m^2 (-0.3 W/m^2 to -0.5 W/m^2) and -0.8 W/m^2 (-0.4 W/m^2 to -1.2 W/m^2) for direct and indirect sulfate forcing, and -0.1 W/m^2 (-0.2 W/m^2 to $+0.1\text{ W/m}^2$) for the sum of biomass and fossil and organic carbonaceous aerosols. The central value for total aerosol forcing is -1.3 W/m^2 (range, -0.6 W/m^2 to -1.9 W/m^2). Results depend primarily on the total aerosol forcing rather than the specific breakdown into different forcing categories. Extreme combinations, such as high climate sensitivity with low aerosol forcing, have very low probability (20).

In the CC case (Fig. 1), both climate sensitivity and aerosol forcing uncertainties are of similar importance. The eventual (equilibrium) commitment could be larger than 1°C (for high sensitivity and low aerosol forcing; low aerosol forcing means a higher value for past total forcing). This result is consistent with Wetherald *et al.* (5) because the Geophysical Fluid Dynamics Laboratory (GFDL) model used by these authors has a high sensitivity (4°C) (14). At the other extreme, the eventual commitment could be less than 0.2°C (for low sensitivity, virtually independent of the magnitude of aerosol forcing).

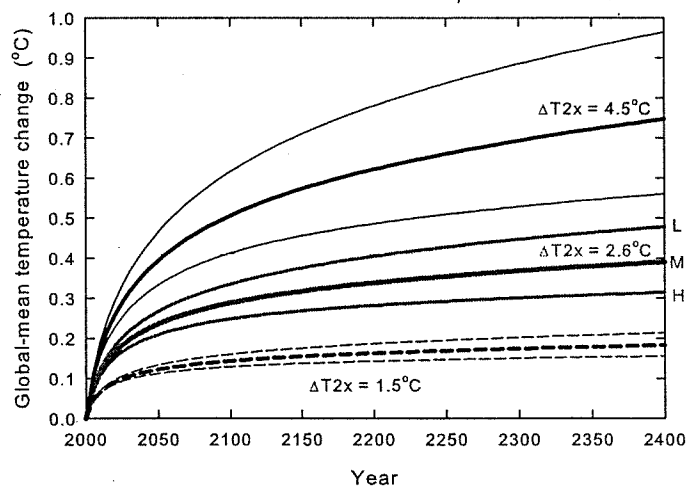


Fig. 1. CC warming commitment (constant concentrations after 2000) for different climate sensitivities and aerosol forcing levels (L, M, and H on the right of the figure indicate low, mid-, and high magnitudes for aerosol forcing, respectively). Values for the central sensitivity value (2.6°C equilibrium warming for a CO₂ doubling) are shown in red.

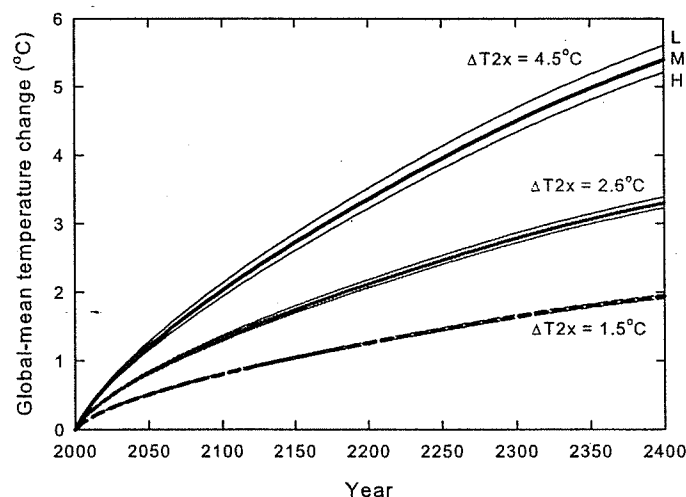


Fig. 2. CE warming commitment (CEs after 2000) for different climate sensitivities and aerosol forcing levels (L, M, and H on the right of the figure indicate low, mid-, and high magnitudes for aerosol forcing, respectively).

Warming commitments for the CE case are much higher and do not tend to any asymptotic limit even on a time scale of millennia (largely because, at CE, CO_2 concentrations continue to grow for many centuries). Climate sensitivity uncertainties are the dominant source of commitment uncertainty. By 2400, the warming ranges from about 2°C (for low sensitivity) to almost 6°C (high sensitivity). The clear message here is that, if we are to avoid future warming of this magnitude, emissions of radiatively active gases will have to be reduced to substantially below present levels.

For the sea level rise commitment results, we have an additional source of uncertainty in the ice melt and unforced contributions to sea level rise. Table S2 shows uncertainties in the CC commitment arising from ocean mixing uncertainties and gives a breakdown of the sea level rise commitment into contributions due to past natural forcing, past anthropogenic forcing, and unforced contributions.

Uncertainties in the CC sea level commitment resulting from uncertainties in ocean

heat uptake arise in two ways. First, the rate of ocean heat uptake affects the rate of atmospheric warming, which affects the rate of melt of land-based ice. Second, the rate of ocean heat uptake directly affects oceanic thermal expansion. For the temperature/melt effect, larger K_z leads to a larger warming commitment, which increases sea level rise. For expansion, larger K_z leads to a greater expansion commitment, also increasing sea level rise. For the commitment, both effects act in concert, in contrast to absolute changes that have compensating effects that reduce overall sensitivity to ocean mixing uncertainties. However, the overall commitment uncertainties arising from K_z uncertainties are small at 7 to 9%.

The breakdown into natural forcing, anthropogenic forcing, and unforced effects shows that unforced effects make a substantial contribution (for the CC case, less so for the CE case). For sea level changes arising from past forcings, anthropogenic forcing dominates.

Climate sensitivity and sulfate aerosol forcing uncertainties for the sea level com-

mitment are shown in Figs. 3 and 4. The CC case, constant concentrations from 2000, is shown in Fig. 3. The central commitment estimate (mid-aerosol forcing, $\Delta T_2 \times = 2.6^\circ\text{C}$, mid-melt) is a continuing rise of around 10 cm/century, of which about 40% is due to unforced effects (table S2) (15). Aerosol uncertainty effects (low, middle, and high values for 1990 forcing) are indicated by the letters to the right of the figure. Results are also shown for sensitivities of $\Delta T_2 \times = 1.5^\circ$ and 4.5°C (mid-melt assumed). Climate sensitivity and aerosol forcing uncertainties are equally important, as shown by the overlapping ranges for different sensitivities. At the extreme high end (high sensitivity, low aerosol forcing, high melt), the rate of rise is almost 30 cm/century (26% due to unforced effects). At the extreme low end, the rate of rise is negligible (with zero unforced changes).

For the CE case (Fig. 4), CE from 2000, the central commitment estimate is a continuing rise of almost 25 cm/century. Approximately 15% of this is due to unforced effects. The lower and upper bounds are around 7 cm/century and more than 50 cm/century. These projections do not include the more catastrophic possibilities of accelerated melt in Greenland or the collapse of the West Antarctic ice sheet, as discussed in the TAR (16).

I considered the conventional (CC) commitment of changes that occur if atmospheric composition is held fixed at present (2000) levels, and the CE commitment for which emissions are fixed at their present levels. These commitments have been quantified for both global-mean temperature and sea level rise. Time-dependent changes are considered rather than just the usual asymptotic or equilibrium commitment.

The CC warming commitment rises steadily to an eventual warming of about 0.2° to more than 1°C . The contribution from past natural forcings exceeds that from past anthropogenic forcing. The corresponding CE warming commitment has no limit even on a time scale of many centuries, primarily because, at CE, CO_2 concentrations continue to rise for a millennium or more. The CE warming commitment in 2400 ranges from 2° to almost 6°C , with most of the commitment due to past anthropogenic forcing. Both climate sensitivity and past aerosol forcing uncertainties are important in determining the CC commitment, whereas climate sensitivity is the main source of uncertainty for the CE commitment.

For sea level rise, both the CC and CE commitments lead to almost linear increases in sea level out to at least 2400 and probably much longer. For the CC commitment, sea level rises at about 10 cm/century (uncertainty range, near zero to about 30 cm/century). Except at the low end of the range, a substantial fraction of this increase arises from unforced contributions to sea level rise (40% in the cen-

Fig. 3. CC sea level rise commitment (constant concentrations after 2000) for different climate sensitivities and aerosol forcing levels (L, M, and H on the right of figure indicate low, mid-, and high magnitudes for aerosol forcing, respectively). The central curves assume best-estimate values for all ice melt parameters. For these curves, aerosol forcing and climate sensitivity uncertainty ranges overlap. For example, the mid-aerosol-mid sensitivity ($\Delta T_2 \times = 2.6^\circ\text{C}$; central red curve) results are very similar to the high-aerosol-high sensitivity ($\Delta T_2 \times = 4.5^\circ\text{C}$; lowest full black curve) results and the low-aerosol-low sensitivity results ($\Delta T_2 \times = 1.5^\circ\text{C}$; top dashed black curve). Extremes spanning sensitivity, aerosol, and melt uncertainties are shown by the bottom and top dotted curves.

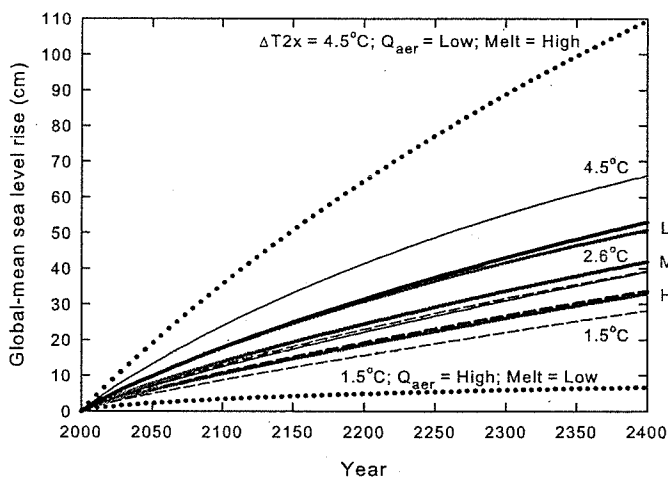
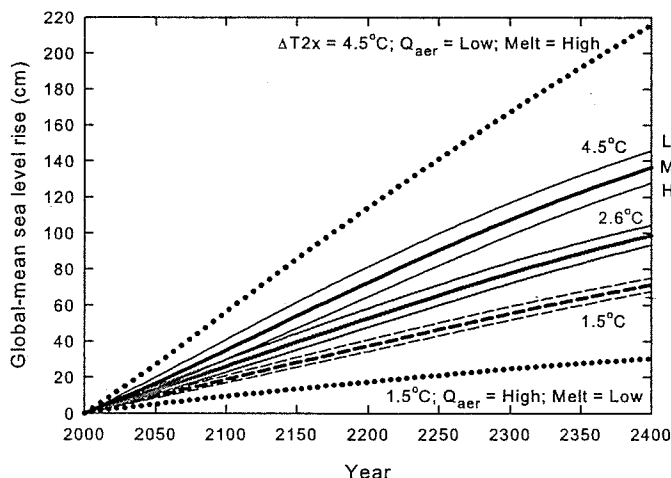


Fig. 4. CE sea level rise commitment (CE after 2000) for different climate sensitivities and aerosol forcing levels (L, M, and H on the right of the figure indicate low, mid-, and high magnitudes for aerosol forcing, respectively). The central curves assume best-estimate values for all ice melt parameters. Extremes spanning sensitivity, aerosol, and melt uncertainties are shown by the bottom and top dashed curves.



tral case). For the CE commitment, sea level rises at about 25 cm/century (uncertainty range, 7 to more than 50 cm/century). The fractions arising from unforced contributions to sea level rise are less than those in the CC case.

The CE results reinforce the common knowledge that, in order to stabilize global-mean temperatures, we eventually need to reduce emissions of greenhouse gases to well below present levels (21). The CC results are potentially more alarming, because they are based on a future scenario that is clearly impossible to achieve and so represent an extreme lower bound to climate change over the next few centuries. For temperature, they show that the inertia of the climate system alone will guarantee continued warming and that this warming may eventually exceed 1°C. For sea level, a continued rise of about 10 cm/century for many centuries is the best estimate. Although such a slow rate may allow many coastal communities to adapt, profound long-term impacts on low-lying island communities and on vulnerable ecosystems (such as coral reefs) seem inevitable.

References and Notes

1. M. L. Hoffert, A. J. Callegari, C.-T. Hsieh, *J. Geophys. Res.* **86**, 6667 (1980).
2. J. Hansen et al., *Science* **229**, 857 (1985).
3. T. M. L. Wigley, M. E. Schlesinger, *Nature* **315**, 649 (1985).
4. T. M. L. Wigley, *Climate Monitor* **13**, 133 (1984).
5. R. T. Wetherald, R. J. Stouffer, K. W. Dixon, *Geophys. Res. Lett.* **28**, 1535 (2001).
6. T. M. L. Wigley, S. C. B. Raper, in *Climate and Sea Level Change: Observations, Projections and Implications*, R. A. Warrick, E. M. Barrow, T. M. L. Wigley, Eds. (Cambridge Univ. Press, Cambridge, 1993), pp. 111–133.
7. R. J. Stouffer, S. Manabe, *J. Clim.* **12**, 2224 (1999).
8. J. Hansen et al., *J. Geophys. Res.* **107**, 4347, 10.1029/2001JD001143 (2002).
9. R. A. Pielke Sr., *Bull. Am. Met. Soc.* **84**, 331 (2003).
10. T. M. L. Wigley, S. C. B. Raper, *Science* **293**, 451 (2001).
11. S. C. B. Raper, T. M. L. Wigley, R. A. Warrick, in *Sea-Level Rise and Coastal Subsidence: Causes, Consequences and Strategies*, J. Milliman, B. U. Haq, Eds. (Kluwer Academic Publishers, Dordrecht, Netherlands, 1996), pp. 11–45.
12. T. M. L. Wigley, S. C. B. Raper, *J. Clim.* **15**, 2945 (2002).
13. U. Cubasch, G. A. Meehl, in *Climate Change 2001: The Scientific Basis*, J. T. Houghton et al., Eds. (Cambridge Univ. Press, Cambridge, 2001), pp. 525–582.
14. S. C. B. Raper, J. M. Gregory, T. J. Osborn, *Clim. Dyn.* **17**, 601 (2001).
15. Materials and methods are available as supporting material on Science Online.
16. J. A. Church, J. M. Gregory, in *Climate Change 2001: The Scientific Basis*, J. T. Houghton et al., Eds. (Cambridge Univ. Press, Cambridge, 2001), pp. 639–693.
17. T. M. L. Wigley, S. C. B. Raper, *Geophys. Res. Lett.*, in press.
18. J. Lean, J. Beer, R. Bradley, *Geophys. Res. Lett.* **22**, 3195 (1995).
19. C. M. Ammann, G. A. Meehl, W. M. Washington, C. S. Zender, *Geophys. Res. Lett.* **30**, 1657, 10.1029/2003GL016875 (2003).
20. This is a sensitivity study and not a probabilistic analysis. Simplistically, if the high climate sensitivity and low forcing extremes are independent and each has a probability of exceedance of 0.05, the probability of both being exceeded is 0.0025. Further constraints may be placed by comparing model simulations with observed climate changes over the past century (22).
21. T. M. L. Wigley, R. Richels, J. A. Edmonds, *Nature* **379**, 240 (1996).
22. C. E. Forest, P. H. Stone, A. P. Sokolov, M. R. Allen, M. D. Webster, *Science* **295**, 113 (2002).
23. Supported in part by the U.S. Environmental Protection Agency under contract no. GS-10F-0299K to Stratus Consulting and by NOAA under grant NA87GP0105. Opinions, findings, or conclusions expressed are those of the author and do not necessarily reflect the views of the funding organization. The National Center for Atmospheric Research is supported by the NSF.

Supporting Online Material

www.sciencemag.org/cgi/content/full/307/5716/1766/DC1

Materials and Methods
Tables S1 and S2

11 August 2004; accepted 10 January 2005
10.1126/science.1103934

How Much More Global Warming and Sea Level Rise?

Gerald A. Meehl,* Warren M. Washington, William D. Collins,
Julie M. Arblaster, Aixue Hu, Lawrence E. Buja,
Warren G. Strand, Haiyan Teng

Two global coupled climate models show that even if the concentrations of greenhouse gases in the atmosphere had been stabilized in the year 2000, we are already committed to further global warming of about another half degree and an additional 320% sea level rise caused by thermal expansion by the end of the 21st century. Projected weakening of the meridional overturning circulation in the North Atlantic Ocean does not lead to a net cooling in Europe. At any given point in time, even if concentrations are stabilized, there is a commitment to future climate changes that will be greater than those we have already observed.

Increases of greenhouse gases (GHGs) in the atmosphere produce a positive radiative forcing of the climate system and a consequent warming of surface temperatures and rising sea level caused by thermal expansion of the warmer seawater, in addition to the contribution from melting glaciers and ice sheets (1, 2). If concentrations of GHGs could be stabilized at some level, the thermal inertia of the climate system would still result in further increases in temperatures, and sea level would continue to rise (2–9). We performed multimember ensemble simulations with two global coupled three-dimensional climate models to quantify

how much more global warming and sea level rise (from thermal expansion) we could experience under several different scenarios.

The Parallel Climate Model (PCM) has been used extensively for climate change experiments (10–15). This model has a relatively low climate sensitivity as compared to other models, with an equilibrium climate sensitivity of 2.1°C and a transient climate response (TCR) (the globally averaged surface air temperature change at the time of CO₂ doubling in a 1% CO₂ increase experiment) of 1.3°C. The former is indicative of likely atmospheric feedbacks in the model, and the latter includes ocean heat uptake and provides an indication of the transient response of the coupled climate system (6, 12). A second global coupled climate model is the newly developed Com-

munity Climate System Model version 3 (CCSM3), with higher horizontal resolution (atmospheric gridpoints roughly every 1.4° as compared to the PCM, with gridpoints about every 2.8°) and improved parameterizations in all components of atmosphere, ocean, sea ice, and land surface (16). The CCSM3 has somewhat higher sensitivity, with an equilibrium climate sensitivity of 2.7°C and TCR of 1.5°C. Both models have about 1° ocean resolution (0.5° in the equatorial tropics), with dynamical sea ice and land surface schemes. These models were run for four- and eight-member ensembles for the PCM and CCSM3, respectively, for each scenario (except for five members for A2 in CCSM3).

The 20th-century simulations for both models include time-evolving changes in forcing from solar, volcanoes, GHGs, tropospheric and stratospheric ozone, and the direct effect of sulfate aerosols (14, 17). Additionally, the CCSM3 includes black carbon distributions scaled by population over the 20th century, with those values scaled by sulfur dioxide emissions for the rest of the future climate simulations. The CCSM3 also uses a different solar forcing data set for the 20th century (18). These 20th-century forcing differences between CCSM3 and PCM are not thought to cause large differences in response in the climate change simulations beyond the year 2000.

The warming in both the PCM and CCSM3 is close to the observed value of about 0.6°C for the 20th century (19), with PCM warming 0.6°C and CCSM3 warming 0.7° (averaged over the period 1980–1999 in relation to 1890–1919). Sea level rises are 3 to 5 cm, respectively, over the 20th century as com-

National Center for Atmospheric Research, Post Office Box 3000, Boulder, CO 80307, USA.

*To whom correspondence should be addressed.
E-mail: meehl@ncar.ucar.edu



900 S.W. Fifth Avenue, Suite 2600
 Portland, Oregon 97204
 main 503.224.3380
 fax 503.220.2480
 www.stoel.com

September 23, 2005

THOMAS R. WOOD
 Direct (503) 294-9396
 trwood@stoel.com

BY FAX AND BY MAIL

Dr. Barry R. Wallerstein
 South Coast AQMD
 21865 Copley Drive
 Diamond Bar, California 91765

Re: Cabrillo Port LNG Terminal

Dear Barry:

Thank you for meeting with BHP last week to discuss the Cabrillo Port Project. We understand based on our conversation that SCAQMD is interested in ensuring that the Cabrillo Port LNG terminal does not import natural gas with a high Btu content as you are concerned that it could impact emissions from stationary sources in the South Coast basin. As Renee Klimczak explained, BHP intends to import natural gas from the Scarborough fields. Scarborough gas is exceptional gas with a higher heating value of approximately 1010 Btus/ft³ and a Wobbe Number of approximately 1356; the specific composition of Scarborough gas is summarized in the table below.

Component Gas	Chemical Formula	Molecular Weight	HHV btu/scf	Composition mole fraction	Composition Mole Wt	HHV btu/scf	HHV btu/lb
Carbon Dioxide	CO ₂	44.010		0.000056	0.00246		
Nitrogen	N ₂	28.013		0.003428	0.09603		
Methane	CH ₄	16.043	1014.2	0.995108	15.96452	1009.25	
Ethane	C ₂ H ₆	30.070	1776.7	0.001130	0.03398	2.01	
Propane	C ₃ H ₈	44.097	2528.7	0.000113	0.00498	0.29	
i-Butane	C ₄ H ₁₀	58.124	3267.2	0.000091	0.00529	0.30	
n-Butane	C ₄ H ₁₀	58.124	3276.7	0.000068	0.00395	0.22	
i-Pentane	C ₅ H ₁₂	72.151	4018.2	0.000000	0.00000	0.00	
n-Pentane	C ₅ H ₁₂	72.151	4027.5	0.000006	0.00043	0.02	
TOTAL				1.00000	16.112	1012.08	24,204.94

Oregon
 Washington
 California
 Utah
 Idaho



Dr. Barry Wallerstein
September 23, 2005
Page 2

However, as we discussed, BHP cannot condition its license on the exclusive importation of Scarborough gas because (1) BHP is only a partial owner of the Scarborough fields and (2) the timelines for development of that project could diverge from the timelines for development of Scarborough—particularly as delays are encountered in permitting Cabrillo Port. Nonetheless, BHP is interested in exploring whether there are ways in which the project can respond to your needs while still allowing BHP the flexibility it requires. Towards that goal, you committed that your staff would provide us with a definition of what constitutes “hot gas” by the week of October 10, 2005. We appreciate that commitment and hope that we can expeditiously bring this matter to a satisfactory resolution.

Please contact Renee Klimczak or myself if you have any questions.

Sincerely,

Thomas R. Wood

cc via email: Amy Zimpfer (EPA Region 9)
Dean Simeroth (CARB)
Gary Yee (CARB)
Mike Villegas (VCAPCD)
Terry Dressler (SBCAPCD)
Cy Oggins (CSLC)
Dwight Sanders (CSLC)



Paul Cort/R9/USEPA/US
09/23/2005 04:57 PM

To Nahid Zoueshtiagh/R9/USEPA/US@EPA, Laura
Yannayon/R9/USEPA/US@EPA, Margaret
Alkon/R9/USEPA/US@EPA

cc

bcc

Subject Fw: CC on Wallerstein letter

fyi

----- Forwarded by Paul Cort/R9/USEPA/US on 09/23/2005 04:56 PM -----



"Wood, Thomas"
<TRWOOD@stoel.com>
09/23/2005 04:53 PM

To Amy Zimpfer/R9/USEPA/US@EPA, Paul
Cort/R9/USEPA/US@EPA, gyee <gyee@arb.ca.gov>,
OGGINSC@slc.ca.gov, sanderd@slc.ca.gov, Dean Simeroth
<dsimerot@arb.ca.gov>, "Mike Villegas (E-mail)"
<mike@vcapcd.org>, dresslert@sbcapcd.org

cc "Renee Klimczak (E-mail)"
<Renee.Klimczak@BHPBilliton.com>, "Thomas Umenhofer
(E-mail)" <tumenhofer@entrix.com>

Subject CC on Wallerstein letter

Attached is a letter to Barry Wallerstein that includes the gas data requested
at last week's EPA meeting.

Tom

Thomas R. Wood
Stoel Rives LLP
Phone: (503) 294-9396
Cell: (503) 349-4845
Fax: (503) 220-2480



wallerstein ltr-9-23-05.pdf

Mike Villegas

om: Wood, Thomas [TRWOOD@stoel.com]
 Sent: Thursday, September 29, 2005 10:29 AM
 To: Chung Liu; Marty Kay
 Cc: renee.klimczak@bhpbilliton.com; Thomas Umenhofer (E-mail); Mike Villegas
 Subject: BHP Cabrillo--Gas Questions

Dear Martin: I apologize for not returning your call yesterday, but it is actually very helpful to have your questions in writing so that I can share the response with others who might be interested. I have rearranged the questions below because the first question in large part answers the second.

Do you have contracts with any alternate LNG suppliers?

BHP is not actively pursuing contracts with other LNG suppliers at this time because the company is still hoping that the permitting process can move along quickly enough that the project can lock in a long term supply of Scarborough gas. Therefore, BHP is not in the precontract stage and certainly has not entered into any contracts for alternate LNG supplies.

What would be the composition, heating value and Wobbe No. of other LNGs you might import if the Scarborough field LNG is not available?

As BHP is focused on obtaining Scarborough gas and is not pursuing other gas supplies, it is not possible to answer this question. Wobbe Number information for gas fields is usually considered proprietary information and is not freely shared. Absent the owner providing you information, it would be necessary to obtain samples and evaluate the gas yourself. BHP has not done this as it hopes not to have to consider other gas supplies. However, it is BHP's understanding that Scarborough gas compares favorably to other supplies.

What ability would the Cabrillo terminal have to treat (NGL removal, nitrogen injection, etc.) these other LNGs to reduce Wobbe number?

The Cabrillo Port terminal has many benefits as the result of being a floating facility 14 miles offshore. However there are also unique space considerations associated with a floating facility. There is no room for the addition of treatment facilities on the floating storage and regasification unit (FSRU). Similarly, there has been no consideration of adding onshore processing facilities as doing so would require a fundamental change in the facility design and permitting. The public has repeatedly requested that we not have an onshore footprint. Adding an onshore facility would contradict BHP's commitment since inception of the project to maintain all of its facilities offshore. Therefore, we do not believe that it is feasible to further treat the LNG received at the terminal.

I hope that I have fully answered your questions. As you can tell, BHP continues to be committed to Scarborough gas.

Tom

Thomas R. Wood
 Stoel Rives LLP
 Phone: (503) 294-9396
 Cell: (503) 349-4845
 Fax: (503) 220-2480

1822

11/9/2005